

Nanochemomechanical assessment of shale: a coupled WDS-indentation analysis

A. Deirieh · J. A. Ortega · F.-J. Ulm ·
Y. Abousleiman

Received: 2 January 2012 / Accepted: 7 August 2012 / Published online: 21 September 2012
© Springer-Verlag 2012

Abstract Establishing the links between the composition, microstructure and mechanics of shale continues to be a formidable challenge for the geomechanics community. In this study, a robust methodology is implemented to access the in situ chemomechanics of this sedimentary rock at micrometer length scales. Massive grids of coupled wave dispersive spectroscopy (WDS) and instrumented indentation experiments were performed over representative material surfaces to accommodate the highly heterogeneous composition and microstructure of shale. The extensive datasets of compositional and mechanical properties were analyzed using multi-variate clustering statistics to determine the attributes of active phases present in shale at microscales. Our chemomechanical analysis confirmed that the porous clay (PC) mechanical phase inferred by statistical indentation corresponds to the clay mineral phase defined strictly on chemical grounds. The characteristic stiffness and hardness behaviors of the PC are realized spatially in regions removed from silt inclusions of quartz and feldspar. At the microscale shared by indentation and WDS experiments, a consistent chemomechanical signature for shale emerges in which the heterogeneities of the PC are captured by the standard deviations of indentation properties and concentrations of chemical elements.

However, these local behaviors are of second order compared to the global trend observed for mean mechanical properties and the clay packing density, which synthesizes the relative volumes of clay and nanoporosity in the material. The coupled statistical indentation and WDS technique represents a viable approach to characterize the chemomechanics of shale and other natural porous composites at a consistent scale below the macroscopic level.

Keywords Cluster modeling · Indentation · Shale · Wave dispersive spectroscopy

1 Introduction

Establishing the links between composition, microstructure and mechanical response continues to be a formidable task toward the understanding of shale. The resolution of these intricate relations is a pressing need for the geomechanics community considering the energy challenges related to this ubiquitous type of sedimentary rock. In addition to serving as geological caps to many hydrocarbon reservoirs, several shale formations have been identified as prolific sources of oil and natural gas [1, 65], as well as host lithologies for the disposal of contaminants such as carbon emissions and nuclear waste [51]. While the knowledge of shale behaviors at macroscales enabled the development of basic drilling strategies and reservoir models, activities such as directional drilling, hydraulic fracturing, and carbon sequestration schemes are requiring experimental programs and modeling frameworks that consider explicitly the highly heterogeneous characteristics of shale.

A necessary approach to fulfill the material science paradigm for shale, that is, to unravel the connections between microstructural features, chemical composition and

A. Deirieh · F.-J. Ulm (✉)
Department of Civil and Environmental Engineering, MIT,
Cambridge, MA 02139, USA
e-mail: ulm@mit.edu

J. A. Ortega
Schlumberger Technology Center, Sugar Land, TX 77478, USA

Y. Abousleiman
Integrated Poromechanics Institute, University of Oklahoma,
Norman, OK 73019, USA

mechanical performance, is to consider this sedimentary rock as a multi-scale material system and its experimental characterization below macroscopic scales. Following the multi-scale structure model suggested in Fig. 1a (see reviews by [26, 28, 45, 56]), the conventional understanding of shale at the macroscale (level II) in terms of its anisotropic poromechanics and transport properties has been supplemented with extensive microstructural information obtained at the level of the clay fabric (level I). Experimental investigations based on advanced imaging [5, 26, 31], X-ray methodologies [35, 36, 61, 63], and small-angle neutron scattering [29] have characterized the textural attributes of the clay matrix in shale as functions of the preferential alignments of clay particles and nanopore pathways. More recently, deployments of nanotechnologies such as atomic force microscopy (AFM) [48] and instrumented indentation [6, 56, 57, 67, 68] have provided direct measurements of mechanical properties for the porous clay fabric (level I) and clay minerals (level 0). Similar studies have also been conducted for the assessment of the organic phase present in the clay matrix of oil- and gas-bearing shales [3, 37, 66]. These direct characterizations of the porous clay matrix offer new contexts for elucidating the behaviors of shale, yet consistent multi-platform characterizations at grain scales are still missing.

In this study, a robust chemomechanical characterization of shale is conducted at micrometer length scales. The characterization employs wave dispersive spectroscopy (WDS) and instrumented indentation experiments to access the chemical composition and mechanics of material volumes of comparable dimensions. To accommodate the heterogeneous structure of shale below the macroscale, extensive grids of coupled WDS and indentation experiments are analyzed using clustering statistics to infer the properties of the relevant mechanical and chemical components. This presentation begins with the introduction of the enabling technologies used to measure the mechanical and chemical attributes of shale with micrometer resolutions and the statistical treatment of the experimental data using cluster modeling techniques. The suits of coupled WDS and indentation experiments and their statistical analysis are then discussed. The generated experimental baseline sheds light into the in situ properties of shale at micrometer scales. The precise definition of the chemomechanical signature of the porous clay phase represents valuable information for multi-scale modeling of this shale component which has been recapitulated until now only through indirect methods.

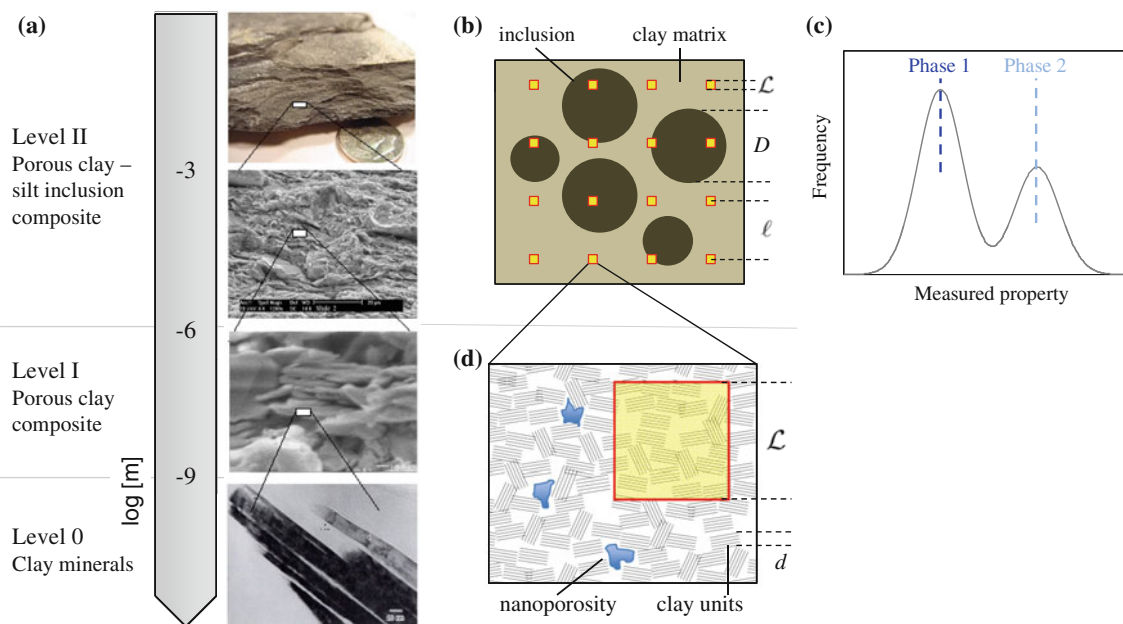


Fig. 1 **a** Multi-scale structure model of shale adapted from [57]. Level 0 corresponds to the scale of clay particles that form the solid matrix in shale. Level I is the scale of the solid clay particles and the nanoporosity that form the porous clay composite. Level II is the macroscopic scale of characteristic length scale in the sub-millimeter and millimeter range, at which shale is composed of the porous clay fabric and silt-size inclusions (mostly quartz and feldspar). The level II and level I images were obtained from scanning electron microscopy (SEM) and the level 0 image was obtained from transmission electron microscopy (TEM) [34], reprinted with the permission of Springer Science and Business Media. **b** Level II of shale represented as a two-phase composite material with its largest heterogeneities of scale $D \gg \mathcal{L}$ and quasi-homogeneous matrix assessed through grid experiments arranged at ℓ equal spacings and with probing sizes \mathcal{L} . **c** Frequency function for a measured property (e.g. mechanical modulus, chemical element) resulting from the analysis of grid indentation or WDS data. **d** Level I of shale comprised of clay units and nanoporosity with characteristic scales $d \ll \mathcal{L}$

2 Methods

This experimental investigation of shale is grounded on the ability to access in situ its chemistry and mechanics at sub-macroscopic length scales. Established techniques such as electron probe microanalysis (EPMA) and instrumented indentation precisely focus on the direct measurements of composition and load-deformation behaviors, respectively, with tunable resolutions reaching some micrometers and sub-micrometers. This section recalls some basic principles of these two enabling technologies, as well as the analysis tools necessary to extend their conventional applications to the study of heterogeneous media. The extensions of wave dispersive spectroscopy and nanoindentation proposed by Ulm et al. to assess engineered and natural composites such as cement, bone, and shale have been reviewed extensively elsewhere (nanomechanics applications [6, 12, 13, 49, 53, 58, 59], chemistry applications [2, 60]). Only the aspects relevant to this novel coupled chemomechanical investigation of shale are presented.

2.1 Instrumented indentation

The indentation experiment consists in pressing an indenter tip of known geometry and mechanical properties orthogonally onto the surface of the investigated material. The applied contact load P and the depth of the indenter with respect to the indented surface h are recorded continuously during the experiment involving a constantly increasing load, a short hold, and a constant unloading. The resulting P – h curve is then interpreted using a continuum-scale mechanical model for a homogeneous infinite half-space to derive the indentation modulus and indentation hardness [43]:

$$M \stackrel{\text{def}}{=} \frac{\sqrt{\pi}}{2} \frac{S}{\sqrt{A_c}} \quad (1)$$

$$H \stackrel{\text{def}}{=} \frac{P}{A_c} \quad (2)$$

where $S = (dP/dh)_{h=h_{\max}}$ is the measured unloading indentation stiffness, A_c the projected area of the indenter on the specimen surface, and P the measured maximum indentation load. The Oliver and Pharr method [42] provides an indirect estimate of the projected area of contact A_c based on the maximum indentation depth h_{\max} . The different indentation parameters can be linked to elastic and strength properties of the material [8, 10, 21, 22, 52]. For instance, the indentation modulus for an isotropic elastic medium corresponds to the plane-stress modulus $M = E/(1 - \nu^2)$, where E is the Young's modulus and ν the Poisson's ratio. Relevant to this investigation is the case of transversely anisotropic elasticity, which is

conventionally how shale is characterized (at least macroscopically). For such material symmetry, the two indentation moduli M_1 , M_3 measured in the directions perpendicular and parallel to the axis of symmetry x_3 are linked to the five elastic constants C_{ij} of the material [16]:

$$M_3 = 2\sqrt{\frac{C_{11}C_{33} - (C_{13})^2}{C_{11}} \left(\frac{1}{C_{44}} + \frac{2}{\sqrt{C_{11}C_{33} + C_{13}}} \right)^{-1}} \quad (3)$$

$$M_1 \approx \sqrt{\frac{\sqrt{C_{11}}(C_{11})^2 - (C_{12})^2}{C_{33}} \frac{M_3}{C_{11}}} \quad (4)$$

The extensive use of instrumented indentation for material characterization has mainly targeted homogeneous materials and thin films.

2.2 Wave dispersive spectroscopy

The chemical analysis of shale in this study employs wave dispersive spectroscopy. This common type of EPMA testing utilizes X-rays emitted from the solicited specimen as a result of a beam of electrons accelerated onto the sample surface to provide compositional information. WDS analysis classifies emitted X-rays based on their wavelengths and offers spatial resolutions on the micrometer range depending on the electron beam energy and sample density [23, 50]. In geology, EPMA techniques have been widely used for the investigation of individual minerals, age determination, and elemental mapping of major constituents in rocks [38]. Image analysis combining back-scattered electron (BSE) micrographs and X-ray maps of representative surfaces of a specimen can deliver microstructural information such as volume fractions and pore/grain size distributions [32], registering successful applications to shale and other sedimentary rocks [18, 54, 55]. WDS spot analysis is used conventionally in conjunction with imaging capabilities in order to isolate a particular grain or phase of interest in rock samples.

2.3 Statistical approach to indentation and WDS experiments for heterogeneous materials

To extend the applications of instrumented indentation and WDS to heterogeneous materials, Ulm and coworkers proposed the so-called grid indentation and WDS techniques, which are based on conducting large arrays of individual experiments on the material surface. Provided adequate choices of experimental parameters, each experiment could be regarded as statistically independent, allowing the application of cluster statistics to interpret the indentation and WDS results. Statistical independence is achieved in the sampling process by setting the grid

spacing ℓ to be larger than the characteristic length scale of the material volume \mathcal{L} being probed experimentally. A large number of tests N are also necessary to avoid sampling effects, demanding the use of sufficiently large surfaces for testing. Capturing the properties of individual phases requires the characteristic length of the probed material volume \mathcal{L} to be adjusted with respect to the heterogeneity dominating the particular scale of observation. At the sub-millimeter scale in shale (level II, Fig. 1b), experiments with a characteristic length scale smaller than the silt-size inclusions $\mathcal{L} \ll D$ will provide access to the properties of the matrix (phase 1) and inclusion materials (phase 2) (Fig. 1c). The assessment of the matrix material as a quasi-homogeneous medium constrains the length scale for the experiment to be larger than the heterogeneities comprised within the matrix. In shale, the porous clay composite (level I, Fig. 1d) is characterized by the presence of fine-sized clay particles and nanopores with characteristic length scales d . If the experiments are designed such that $d \ll \mathcal{L}$, the chemomechanical experiments will sense the on-average (homogenized) responses of the particular material volumes in each location of the sample surface.

The applications of grid indentation and WDS techniques entail performing large sets of experiments. We resort to multi-variate cluster modeling for the statistical analysis of the generated mechanical and chemical data. Cluster modeling provides a rational means for determining the most likely number of components or clusters associated with the multi-variate data via likelihood criteria. The cluster modeling of grid data considers each set of experimental properties \mathbf{y}_j to be a realization of the multi-dimensional array $\mathbf{y} = (\mathbf{y}_1^T, \dots, \mathbf{y}_N^T)$, where N is the total number of experiments. Assuming a mixture of normal components, the probability density function $f(\mathbf{y}_j)$ of the observed data \mathbf{y}_j with a g component mixture is:

$$f(\mathbf{y}_j; \Psi) = \sum_{i=1}^g \pi_i c(\mathbf{y}_j; \boldsymbol{\mu}_i, \boldsymbol{\Sigma}_i) \quad (5)$$

where π_i are the mix proportions with $0 \leq \pi_i \leq 1$ and $\sum_{i=1}^g \pi_i = 1$, and $\Psi = (\pi_1, \dots, \pi_{g-1}, \boldsymbol{\xi}^T)^T$ with $\boldsymbol{\xi}$ containing the (unknown) elements of the component means $\boldsymbol{\mu}_i$ and variance–covariance matrices $\boldsymbol{\Sigma}_i$. The estimates of mix proportion are treated as volume fractions within the context of the quantification of the portion of spot analyses assigned to a particular component. The volume fraction estimate is given by $\pi_i = (\sum_{j=1}^N \tau_{ij})/N$, where τ_{ij} represents the posterior probability that \mathbf{y}_j belongs to the i th g component. The function $c(\mathbf{y}_j; \boldsymbol{\mu}_i, \boldsymbol{\Sigma}_i)$ corresponds to the multi-variate normal density:

$$c(\mathbf{y}_j; \boldsymbol{\mu}_i, \boldsymbol{\Sigma}_i) = \frac{1}{\sqrt{2\pi}} (\boldsymbol{\Sigma}_i)^{-\frac{1}{2}} \exp \left[-\frac{1}{2} (\mathbf{y}_j - \boldsymbol{\mu}_i)^T (\boldsymbol{\Sigma}_i)^{-1} (\mathbf{y}_j - \boldsymbol{\mu}_i) \right] \quad (6)$$

Assuming that experiments $\mathbf{y}_1, \dots, \mathbf{y}_N$ are independent and identically distributed realizations, the log likelihood function for Ψ is [40]:

$$\log L(\Psi) = \sum_{j=1}^N \log f(\mathbf{y}_j; \Psi) \quad (7)$$

The maximum likelihood approach via the expectation–maximization (ML–EM) algorithm [17, 39] allows for an efficient solution of (7). The multi-variate cluster modeling was accomplished in this work using MCLUST, a R based software package for normal mixture modeling and model-based clustering [20]. The algorithm determines the optimal number of normal mixture distributions which best describes the experimental data using a Bayesian information criterion (BIC).

2.4 Interpretation of cluster modeling results

The statistical analysis of the grid indentation and WDS data using clustering modeling aims at identifying the active mechanical and chemical components at the scale of observation. For grid indentation data, cluster modeling involves two mechanical variables, the indentation modulus and hardness. The interpretation of indentation clustering results, already pursued by Ulm and Abousleiman [6, 56], will be revisited and thoroughly discussed later in this work. In comparison to the interpretation of mechanical results, the interpretation of clustering results from WDS data is more involved given the number of chemical elements being measured in the EPMA experiments. After the selection of a suitable set of chemical elements that optimally describes the major and minor mineral components typically found in shale, a total of seven elements (Si, Al, Fe, K, Mg, Ca, Na) were used for the chemical characterization of the materials considered in this study. These elements were inputs to the cluster modeling for classifying the individual WDS spot analyses into chemical components with similar compositions.

To aid in the interpretation of grid WDS data and clustering results, Deirieh et al. [15] designed a series of elemental projections of the variable space associated with the WDS experiments on shale materials. Each WDS test represents a point in the multi-dimensional space defined by the base dimensions of selected chemical elements. Table 1 lists the chemical compositions of common non-clay minerals present in shale in terms of their chemical formulas and corresponding atomic percentages. The projections of data in the Al–Si and Al/Si – K + Ca + Na

Table 1 Chemical compositions of non-clay minerals expressed as atomic percentages

Mineral	Chemical formula	Si	Al	Al/Si	K + Ca + Na
Quartz	SiO ₂	33.3	0		0
Alkali feldspar	(Na, K)AlSi ₃ O ₈	23.0	7.7	0.3	7.7
Plagioclase feldspar	NaAlSi ₃ O ₈ –CaAl ₂ Si ₂ O ₈	23.0–15.4	7.7–15.4	0.3–1.0	7.7

Mineral	Chemical formula	Ca	Mg	Fe
Calcite	CaCO ₃	20	0	0
Magnesite	MgCO ₃	0	20	0
Siderite	FeCO ₃	0	0	20
Dolomite	CaMg(CO ₃) ₂	10	10	0
Hematite	Fe ₂ O ₃	0	0	40

The combinations of these elemental representations are used for constructing the visual interpretations of WDS data displayed in Fig. 2

spaces are useful to identify framework silicates such as quartz and feldspars, as shown in Fig. 2a, b. A well-defined site in the Al–Si variable space is recognized for quartz, with atomic percentages Si = 33.3, Al = 0. For feldspars, a site in the K + Ca + Na dimension is found at an atomic percent value of 7.7. The use of the elements Ca, Mg, and Fe helps characterizing carbonate minerals. Figure 2c, d show projections in the spaces Fe–Si and Ca–Mg used for the interpretation of siderite, magnesite, dolomite, and calcite. The projection Fe–Si can also aid in the identification of hematite.

The characterization of clay minerals is a more challenging task. The standard EPMA experiment cannot be used to study the compositional features of the small-sized clay structures due to the larger length scales of the probed

material volumes (or microvolumes). The proposed experiments can only resolve the on-average clay chemistries across different locations on the shale matrix. To this end, Fig. 2b compiles graphically the chemical compositions of common clay minerals found in shale: illite, montmorillonite, mixed-layer illite–smectite, and kaolinite. Representative compositions for these minerals gathered from the open literature [14, 41, 62] were transformed in atomic percentages, and the results are displayed in the Al/Si – K + Ca + Na space. Figure 2b illustrates the variabilities in chemical constitution of the considered clay minerals. The proposed variable space enables the distinction between 1:1 and 2:1 clay groups, where a clear site for kaolinite is distinguished from illite and smectite sites. The identification of known sites for clays and non-clay minerals in the proposed variable spaces will aid in the interpretation of the cluster modeling of WDS data. The most likely chemical components identified through clustering statistics represent components with similar chemistry within the shale material. Each of the clusters of chemical data will be linked to the particular sites described in Fig. 2 as means to decode chemical signatures. The results from statistical WDS obtained for two shale materials will be used in conjunction with those from statistical indentation to unveil the in situ chemomechanical properties shale at micrometer length scales.

3 Experimental program

3.1 Shale materials

Our chemomechanical study was conducted on two materials, shales S3 and S7, which were provided by the GeoGenome Industry Consortium (G2IC). Although information about the geologic origin of the cored samples was not

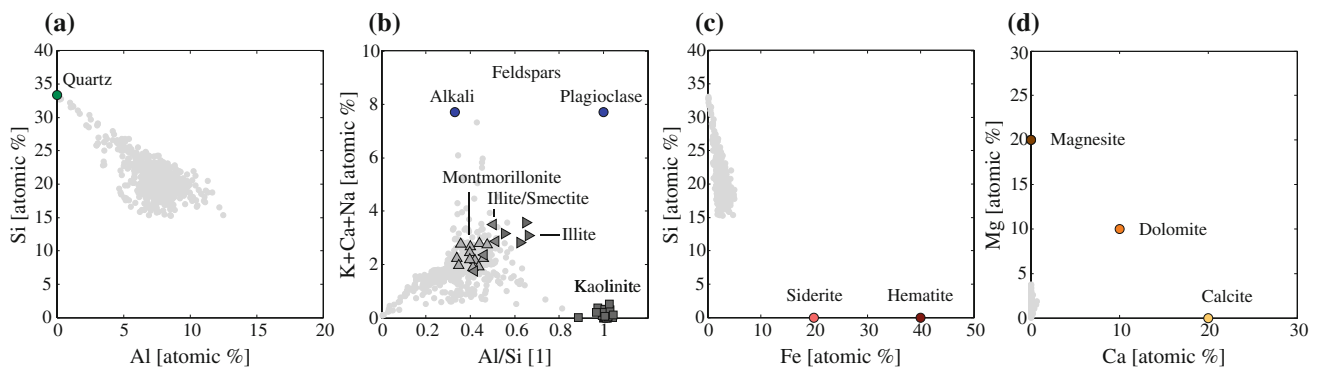


Fig. 2 Grid WDS data for shale S3 (experiment S3–W1) presented on 2-D projections of elemental atomic percentages. The theoretical atomic percentages for non-clay minerals from Table 1 and experimental observations for common clay minerals in shale from [14, 41, 62] are also displayed. **a** Al–Si space helps identify quartz data. **b** Al/Si – K + Ca + Na space separates feldspar and clay minerals. **c** Fe–Si space separates siderite and hematite minerals. **d** Ca–Mg space separates carbonate minerals such as calcite, dolomite, and magnesite

disclosed, these shale materials belong to a comprehensive database of samples from rock formations with little organic content that serve as geological caps to hydrocarbon reservoirs (see reviews in [6, 45, 46]). Tables 2 and 3 compile relevant experimental data regarding the composition of shales S3 and S7 obtained from mineralogy, porosity, and density tests. Based on these data, volume fraction estimates of individual mineral components can be estimated. For a particular mineral k , its volume fraction is determined by:

$$f_k = (1 - \phi) \frac{m_k / \rho_k}{\sum_{i=1}^n m_i / \rho_i} \quad (8)$$

where m_i is the mass fraction of the solid constituent provided by X-ray diffraction (XRD), ρ_i the corresponding mineral density available from the open literature, and ϕ the porosity of the shale rock. In addition to the direct measurement through mercury intrusion porosimetry (MIP), an alternative estimate of porosity can be calculated employing bulk density and mineralogy information. The dominating volume fraction in the compositions of the two shale materials is that of clay minerals (mainly illite, smectite, and kaolinite totaling $f^{\text{clay}} = 0.64\text{--}0.65$), compared to the contributions of non-clay minerals (quartz, feldspar, and others totaling $f^{\text{inc}} = 0.28\text{--}0.29$) and porosity $\phi = 0.07$. The characteristic pore throat radii for these shale samples estimated through MIP tests are on the order of a few nanometers [6]. This characteristic size of the pore space and the known sub-micrometer dimensions of clay minerals justify the consideration of the porous clay phase

Table 2 Mineralogy information in mass percents of shale samples provided by the GeoGenome Industry Consortium

Sample	Quartz	Feldspar	Other inclusions	Kaolinite	2:1 clays	Other clays
S3	21.2	3.5	5.6	9.0	60.5	0.2
S7	18.5	7.2	5.6	37.9	30.8	0.0

The mineralogy data were obtained by X-ray diffraction. non-clay minerals include framework silicates (quartz, feldspar) and others (carbonates, hematite, pyrite, and anhydrite). Clay minerals include kaolinite, 2:1 clays (illites, smectites), and other clays (chlorite, glauconite, biotite, serpentine, and berthierine)

Table 3 Porosity data obtained by mercury intrusion porosimetry (MIP)

Sample	Porosity, ϕ [%]	Bulk density [g/cm ³]	Clay percent, f^{clay}	Inclusion percent, f^{inc}
S3	7	2.55	65	28
S7	7	2.51	64	29

Clay and inclusion (non-clay) volume percents were calculated based on the measured porosity, the solid mass fractions from XRD, and corresponding mineral densities

(level I) at the length scale of micrometers as postulated in the multi-scale structure model of Fig. 1.

For indentation and WDS experiments, laboratory-size samples of 10 mm diameter and 5 mm height were trimmed from well-preserved shale specimens that were kept in desiccators containing salt solutions to maintain adequate humidity conditions. The trimming of the samples was directed to expose the surface normal to the natural bedding plane of the materials. The samples were mounted on stainless steel disks for machine handling. The surface preparation included a coarse polishing on 400 grit hard perforated pads (TexMet P, Buehler) and an oil-based diamond suspension in order to avoid chemical reactions. This first step provided a leveled surface parallel to the mounting disk. The second step consisted of a dry polishing step using a series of aluminum oxide abrasive disks (FibrMet, Buehler), with abrasive grain sizes ranging between 9 and 1 μm . Samples were ultrasonicated in *n*-decane solution between polishing steps. From AFM characterization, the root-mean-squared (RSM) roughness obtained for sister samples was on the order of 30–150 nm, which compares adequately with previous studies [6]. For WDS analysis, shale samples were coated with a 20 nm layer of carbon to prevent charge built-up during electron bombardment while optimizing the X-ray intensity levels in the experiments [23, 50].

3.2 Coupled grid indentation and WDS experiments

The implementation of the grid indentation and WDS techniques for the chemomechanical study of shale followed the experimental program detailed in Table 4. A total of four different surface locations were chosen for the coupled chemomechanical testing. The first two surfaces associated with experiments S3-1 and S3-2 correspond to material regions with random distributions of inclusions (mostly quartz and feldspars) with moderate particle sizes. These surfaces were deemed to be representative of the overall material makeup for shale S3. In contrast, the remaining two surfaces associated with experiments S3-3 and S7-1 exhibit feldspar and quartz grains, respectively, with notoriously large dimensions. In addition to grid indentation and WDS experiments, these two surface locations were solicited using BSE microscopy and X-ray mapping for visual assessments. The resulting battery of experiments will shed light on the links between grid indentation and WDS test results and microstructural features at grain interfaces.

The experiments were performed in square grids of evenly spaced measurements. Grid spacings of 5 and 10 μm provide the necessary separation between indents and WDS spot analyses. The resulting grids of tests covered surfaces between 125×125 and $260 \times 260 \mu\text{m}^2$.

Table 4 Experimental program of grid indentation and WDS experiments conducted over four surface locations in shales S3 and S7

Sample	Surface location	Technique	Grid experiment	Array	Grid spacing, ℓ [μm]
S3	1	Indentation	S3-I1	25×25	5
		WDS	S3-W1	25×25	5
	2	Indentation	S3-I2	20×20	10
		WDS	S3-W2	20×20	10
	3	Indentation	S3-I3	31×31	5
		WDS	S3-W3	31×31	5
S7	1	X-ray/BSE	S3-X3		
		Indentation	S7-I1	26×26	10
		WDS	S7-W1	26×26	10
		X-ray/BSE	S7-X1		

Each grid experiment $S\alpha - T\beta$ is labeled by $\alpha = [3, 7]$ denoting the shale material, T the experimental technique (indentation, WDS, X-ray/BSE), and β the particular surface location

The grid of WDS spot analyses was performed with a slight offset from the grid of indentations to avoid the created local deformation from indents which may interfere with the chemical measurements.

The coupling of chemical and mechanical techniques has already been implemented in studies of composite materials. A combination of SEM, confocal laser-scanning microscopy (CLSM), and AFM testing was used for estimating elastic properties in organic-rich shale [3]. EPMA and indentation techniques were implemented in studies of cement pastes [11, 27], in which chemical information from scanning electron microscopy and energy dispersive spectra (SEM-EDS) was linked to mechanical information. However, only in the former study, the microvolumes probed by the two techniques were of similar magnitudes. The precision in these studies gained from the visual assessments, EPMA, and indentation test spots resulted in isolating particular material phases for later analysis. The grid WDS technique replaces the need for imaging by the use of statistical analysis to treat the large datasets of chemical measurements and capture the compositional makeup of the investigated material. The clustering results of grid WDS data can be then linked to those of overlapping grid indentations. In principle, the indentation and WDS data could be interpreted using a multi-variate clustering model in which all variables (stiffness, hardness, and the various chemical elements) are considered simultaneously. Although such methodology is under development, the separate modeling of indentation and WDS data and later coupling of results will become advantageous in the study of shale as they provide different insights into the behaviors of this material at sub-macroscopic length scales.

The indentation experiments on shale were performed in a CSM Nanoindenter (CSM Instruments, Switzerland). Each indentation test involved the application of a trapezoidal loading function, with a linear increase to 4.8 mN in 30 s, followed by a holding phase for 10 s, and a linear unloading phase in 30 s. A Berkovich indenter (three-sided pyramid) was used in the experiments, and the calibration of the contact area function was based on a fused silica standard. The mechanical properties probed in indentation experiments correspond to drained responses. For indentation depths of nanometer or micrometer range and the prescribed loading rates, pore pressures are dissipated over the probed microvolumes. The chemical data were collected on a JEOL JXA-733 superprobe (JEOL Ltd., Japan), equipped with a WDS spectrometer operating at an accelerating voltage of 15 kV and beam current of 10 nA. The operating distance was set to 10 mm. A total of seven elements were deemed relevant for the characterization of the shale specimens considered in this study, with calibrations made on their standard oxide specimens: silicon, aluminum, iron, sodium, magnesium, potassium, and calcium. Other elements such as sulfur, manganese, and titanium were measured but not included in the statistical analysis given their presence in small quantities (<0.2 % by weight). Matrix corrections accounting for the atomic number, absorption, and fluorescence followed the ZAF method. Using the same experimental platform, BSE images and X-ray maps of several elements were also recorded for experiments S3-X3 and S7-X1.

An important consideration for the coupling of indentation and WDS experiments is the adequate comparison of material volumes probed by each technique. Monte Carlo simulations of the WDS experiment were performed using CASINO, an open-source simulation software [19], to assess the characteristic size of the interaction volume between bombarded electrons and the material sample. The simulations were performed on common shale constituents such as quartz and illite and employed the experimental parameters used in laboratory tests. Figure 3a displays a cross-section of illite sample and the computed electron trajectories. The Monte Carlo simulations showed volumes of interaction with characteristic sizes of $\mathcal{L} \approx 2-3 \mu\text{m}$. The length scale associated with the WDS experiment matches that of instrumented indentation defined by the maximum indentation depth (Fig. 3b). Finite element simulations for indentation testing using a Berkovich probe have shown that the measured elastic response during testing corresponds to a material volume that is approximately 3–5 times the characteristic depth of indentation [13, 33]. With average maximum indentation depths of approximately $h_{\text{max}} \approx 700-900 \text{ nm}$ for the indentation experiments in Table 5, the material domains sensed by indentation are on the order of 2–4 μm . The length scale defined for our WDS and indentation experiments of a

few micrometers suggests that the chemical and mechanical assessments are to resolve the fine-grained clay matrix (level I) through on-average properties. Nevertheless, the grid experiments and their statistical analysis will resolve the chemical and mechanical contrasts between the silt-size inclusions and the porous clay matrix.

4 Results

The results from cluster modeling of grid indentation and WDS experiments determine the types of components that are identified in shale by each methodology: mechanical active components from statistical indentation and

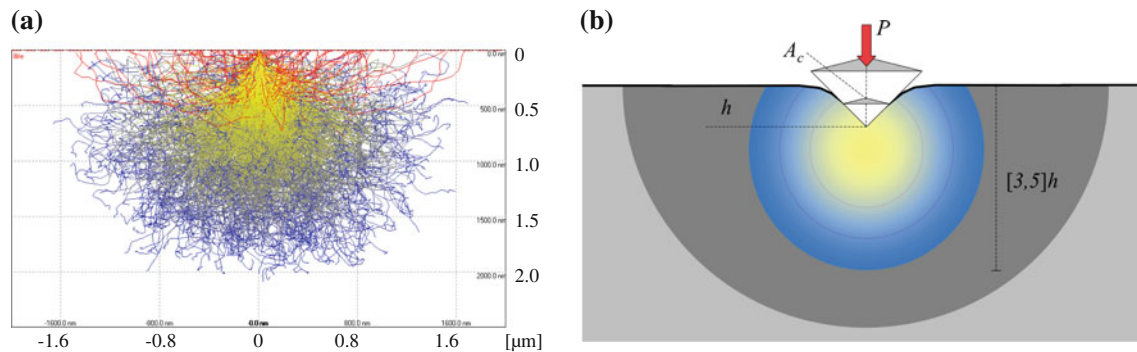


Fig. 3 **a** Monte Carlo simulations run in CASINO of the electron trajectories in WDS experiments performed on a shale mineral constituent: illite [$\text{K}_{1.5}\text{Al}_4(\text{Si}_{6.5}, \text{Al}_{1.5})\text{O}_{20}(\text{OH})_4$, $\rho = 2.80 \text{ g/cm}^3$]. The trajectories reaching up to 0.5 microns are mainly back-scattered electrons, which result from elastic scattering events. Trajectories beyond 0.5 microns correspond to low and high energies. **b** Characterization of intrinsic phase properties from an indentation experiment

Table 5 Summary of cluster analysis for grid indentation experiments on shales S3 and S7

Experiment	S3-I1				S3-I2		
Phase	1	2	3	4	1	2	3
Modulus, M_3^μ [GPa]	12.44	20.34	30.43	108.08	11.95	16.13	28.59
Modulus, M_3^σ [GPa]	3.11	5.67	9.00	35.81	2.04	2.81	10.28
Hardness, H_3^μ [GPa]	0.32	0.76	3.19	17.53	0.39	0.63	3.39
Hardness, H_3^σ [GPa]	0.13	0.27	1.65	7.26	0.10	0.18	1.90
Correlation, $\rho_{M,H}$ [1]	0.89	0.46	0.79	0.80	0.87	0.62	0.84
Allocation rate, A [1]	0.95	0.84	0.96	1.00	0.90	0.86	0.98
Depth, h_{\max}^μ [nm]	931	585	331	162	828	634	342
Depth, h_{\max}^σ [nm]	221	91	61	22	109	70	69
Volume fraction [%]	57	18	20	5	64	30	6
No. data	305	88	93	25	196	77	16
Experiment	S3-I3			S7-I1			
Phase	1	2	3	1	2	3	4
Modulus, M_3^μ [GPa]	15.14	27.23	82.87	14.36	24.48	73.53	143.66
Modulus, M_3^σ [GPa]	4.54	6.32	36.66	3.15	5.96	27.91	13.01
Hardness, H_3^μ [GPa]	0.50	1.35	11.01	0.42	0.79	8.28	16.56
Hardness, H_3^σ [GPa]	0.23	0.63	6.95	0.14	0.27	3.93	2.22
Correlation, $\rho_{M,H}$ [1]	0.89	0.28	0.94	0.84	0.59	0.78	0.56
Allocation rate, A [1]	0.96	0.84	0.99	0.92	0.91	0.98	0.95
Depth, h_{\max}^μ [nm]	787	481	215	813	569	222	157
Depth, h_{\max}^σ [nm]	244	116	52	175	93	44	7
Volume fraction [%]	50	15	34	39	24	19	18
No. data	214	66	139	247	134	111	110

The notations μ and σ correspond to the mean and standard deviation of the given property. The Pearson correlation coefficient $\rho_{M,H}$ was calculated based on the covariance and standard deviations of stiffness M_3 and hardness H_3 data assigned to each phase through cluster modeling. The values for the number of measured data (no. data), indentation depth h_{\max} , volume fraction, and allocation rate A are also listed

chemical components from statistical WDS. The experimental evidence that is brought forward by each method will be synthesized in Sect. 5 to establish the chemomechanical signature of shale at micrometer scales.

4.1 Statistical indentation analysis

The results of the statistical indentation assessments of shales S3 and S7 are compiled in Table 5. By means of illustration, this section describes the analysis of the grid indentation data gathered for experiment S3–I1. Figure 4 summarizes graphically the results of cluster analysis for this experiment. Via the BIC criterion, four mechanical components were identified from the clustering of indentation modulus and hardness measurements as shown in Fig. 4a, b. The term mechanical component is understood as each of the clusters recognized by the multi-variate statistical approach based on the underlying elasticity and hardness characteristics. A priori, these mechanical components active in the response of shale at micrometer and

sub-micrometer scales are not yet linked to particular material chemistries. On-average modulus and hardness properties display increasing values, ranging between those of cluster 1 (with the lowest values) and cluster 4 (with the highest values). In addition, the correlation between indentation properties, quantified by the correlation coefficient $\rho_{M,H}$ (Table 5), is consistently positive for each phase. This can be inferred graphically by the positive slopes displayed by the principal axes of the ellipses representing the modeled normal distributions. Figure 4c shows typical indentation responses measured for components 1 and 4. The indentation load-depth curve representative of component 1 exhibits a larger maximum depth, a significant amount of creep during the holding phase regime of load application, and a large plastic deformation upon unloading. In contrast, the deformation response of the experiment linked to component 4 displays less plastic behavior upon unloading and relatively little creep. The behaviors illustrated by the sample tests have been previously documented in [6, 56] for grid indentation data on

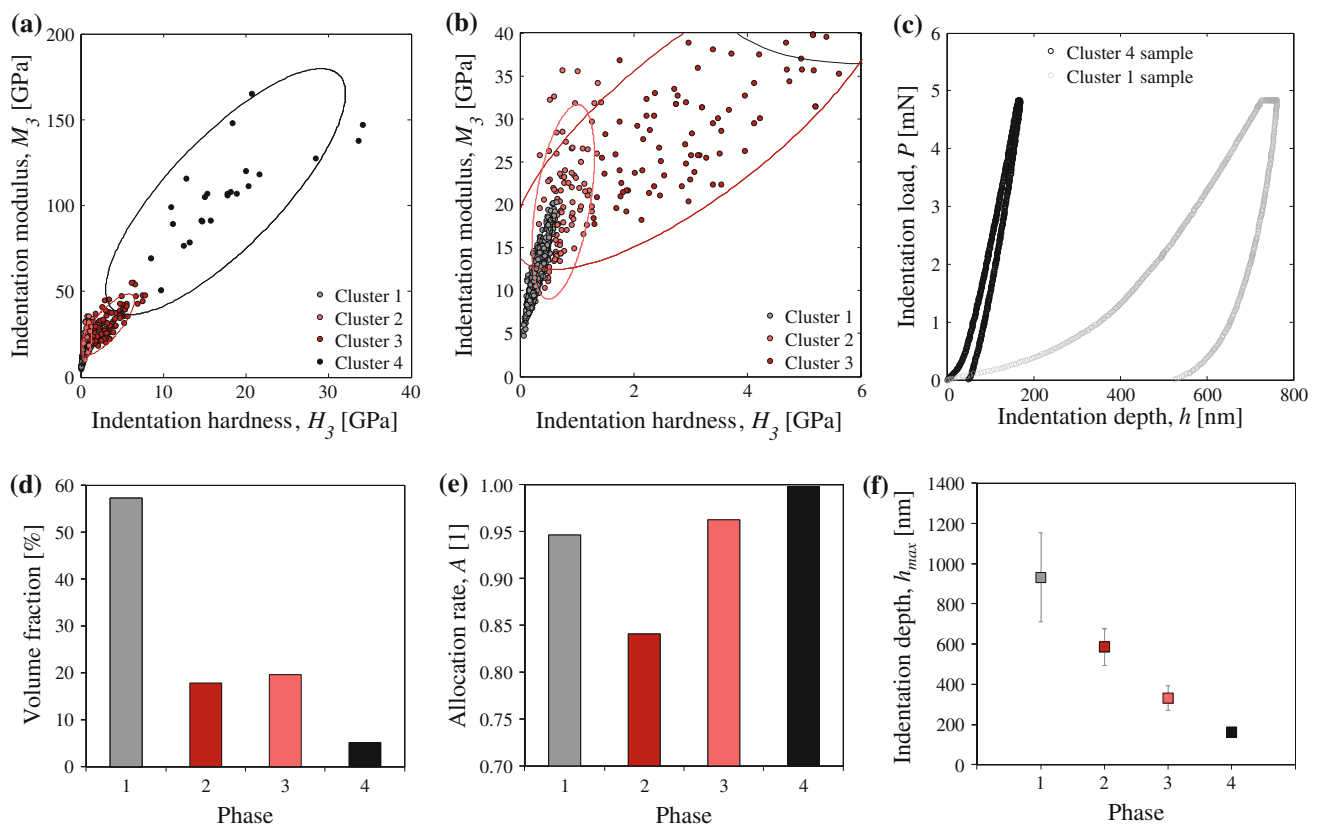


Fig. 4 Cluster analysis of the grid indentation data for experiment S3–I1. **a** The cluster modeling of the indentation modulus and hardness data identified four mechanical components. **b** Close-up of the indentation data and cluster modeling presented in **a**. **c** Representative indentation responses measured in the grid experiment S3–I1. The load–depth curves were recorded for tests clustered in components 1 and 4. The indentation modulus and hardness inferred from these experimental curves are $M_3 = 14.7$, $H_3 = 0.43$ GPa for the experiment assigned to cluster 1, and $M_3 = 92.4$, $H_3 = 16.1$ GPa for the experiment assigned to cluster 4. **d**, **e** Volume fractions and allocation rates for each of the mechanical components identified by the cluster model in **a**. **f** Mean and standard deviation values of the maximum indentation depths corresponding to each mechanical component

other shale samples. Two other important trends emerging from the statistical clustering results are associated with volume fractions and allocation rates. Component 1 displays the largest volume fraction compared to components 2–4 (Fig. 4d). Moreover, some of the highest values of allocation rate for experiment S3–I1 (Fig. 4e) and the rest of experiments in Table 4 were assigned to components 1 and 3 (or 4, whichever is the component with the highest modulus and hardness values). This entails that the data for these two bounding cases of mechanical components are better clustered by the statistical approach.

With each indentation experiment properly assigned to the four mechanical components, estimates of maximum indentation depths for each component are displayed in Fig. 4f. The average indentation response for the data clustered in component 1 is $h_{\max} = 931 \pm 221$ nm. For components 2–4, the indentation depths are lower, reaching 162 ± 22 nm for component 4. For component 1, the indentation depth of slightly <1 μm already hints toward the assessment of the in situ properties of the composite consisting of clay minerals and nanoporosity. It will be shown that the data associated to components with similar characteristics as cluster 4 correspond to non-clay inclusions. The trends discussed in this section apply to the remaining sets of grid indentation experiments.

4.2 Statistical WDS analysis

The chemical assessment of shale using the statistical WDS technique is detailed in this section using as reference the results for experiment S3–W1. This grid experiment was performed over the same location used for experiment S3–I1. The WDS data for experiment S3–W1 prior to cluster modeling were already displayed in Fig. 2. The implementation of cluster modeling yielded the results graphically displayed in Fig. 5 for the four elemental projections proposed in Sect. 2. The application of the BIC criterion determined that nine clusters describe the multi-variate WDS data gathered for grid S3–W1. Figure 6 and Table 6 compile the assessments of volume fractions, allocation rates, and the statistics of yield totals associated with the nine chemical components. Table 6 also lists the chemical properties for each cluster in terms of mean values Λ_i^{μ} and standard deviations Λ_i^{σ} , where $i = [1, g]$ components and $\Lambda = [\text{Si}, \text{Al}, \text{Fe}, \text{K}, \text{Mg}, \text{Ca}, \text{Na}]$.

Two types of clusters based on their form are recognized in the projection spaces shown in Fig. 5: poles and ligands. A pole represents a cluster with an intense grouping of data around a mean position. Pole-type clusters are interpreted as quasi-homogeneous phases that match a particular chemistry known to be present in shale. For experiment S3–W1, components 1–7 are identified as poles. Figure 5a

reveals that component 7 is located in the region of quartz, with a silicon content of $\text{Si}_7 = 31.6 \pm 1.1$ %. The values for the remaining elemental mean properties are low (atomic percentages below 2.0). Components 1–6 are located in the elemental space expected for clay minerals as shown in Fig. 5b. The chemical data linked to these phases exhibit pronounced spreads in comparison with the quartz pole. The a priori knowledge of the expected variabilities in clay mineralogy for different clay groups (e.g. 1:1 and 2:1 clays) warrants the interpretation of components 1 through 6 as clay poles. The characteristic size of clay minerals below the scale of the WDS experiment hints toward a measurement of the on-average composition of clay minerals contained within the excited microvolume. The locations of clay poles in the Al/Si – K + Ca + Na projection in Fig. 5b and their comparison to the clay data from the open literature presented in Fig. 2b reveal a clay matrix dominated by 2:1 clay minerals. This observation is consistent with the mineralogy assessment by XRD tests presented in Table 3. A more detailed analysis of the clay mineralogy in the framework of the statistical WDS method will be presented in Sect. 5.

The identification of components 1–6 as clay dominated is also corroborated by their large volume fractions, totaling 84 % of the material volume. The statistical information related to the yield totals and allocation rates further complements the interpretations of the quartz and clay poles. The deviation of yield totals from the ideal value of 100 % can be related to the experiment not capturing specific elements, as it is the case for components 1 through 6. Their low yield totals ($T_{1-6}^t < 95$ %) are the results of not measuring hydrogen, which is present in the clay structures as bound water or hydroxyl groups. The associated variabilities of yield totals for these components ($T_{1-6}^{\sigma} = 3.3$ – 5.4 %) are some of the largest in the set, which may be indicative of the chemical diversity of clays. In contrast, the yield total statistics for the quartz component (cluster 7) display the highest mean value and the lowest standard deviation from the set, which agree with the chemical nature of quartz with little variances due to impurities or substitutions. The allocation rate for the quartz component is also the highest in the set ($A_7 = 1$). These high values convey the high probabilities for each of the WDS experiments belonging to a chemically distinct phase.

The second form of clusters determined for experiment S3–W1 is the presence of ligands. A ligand is defined as a cluster associated with the mixture between two chemical phases. These clusters can be identified visually as components that span between poles or known mineral sites in the elemental variable space for shale. The inspection of Fig. 5 reveals the presence of two ligands: cluster 8 linking quartz and clay components (Fig. 5a), and cluster 9 linking

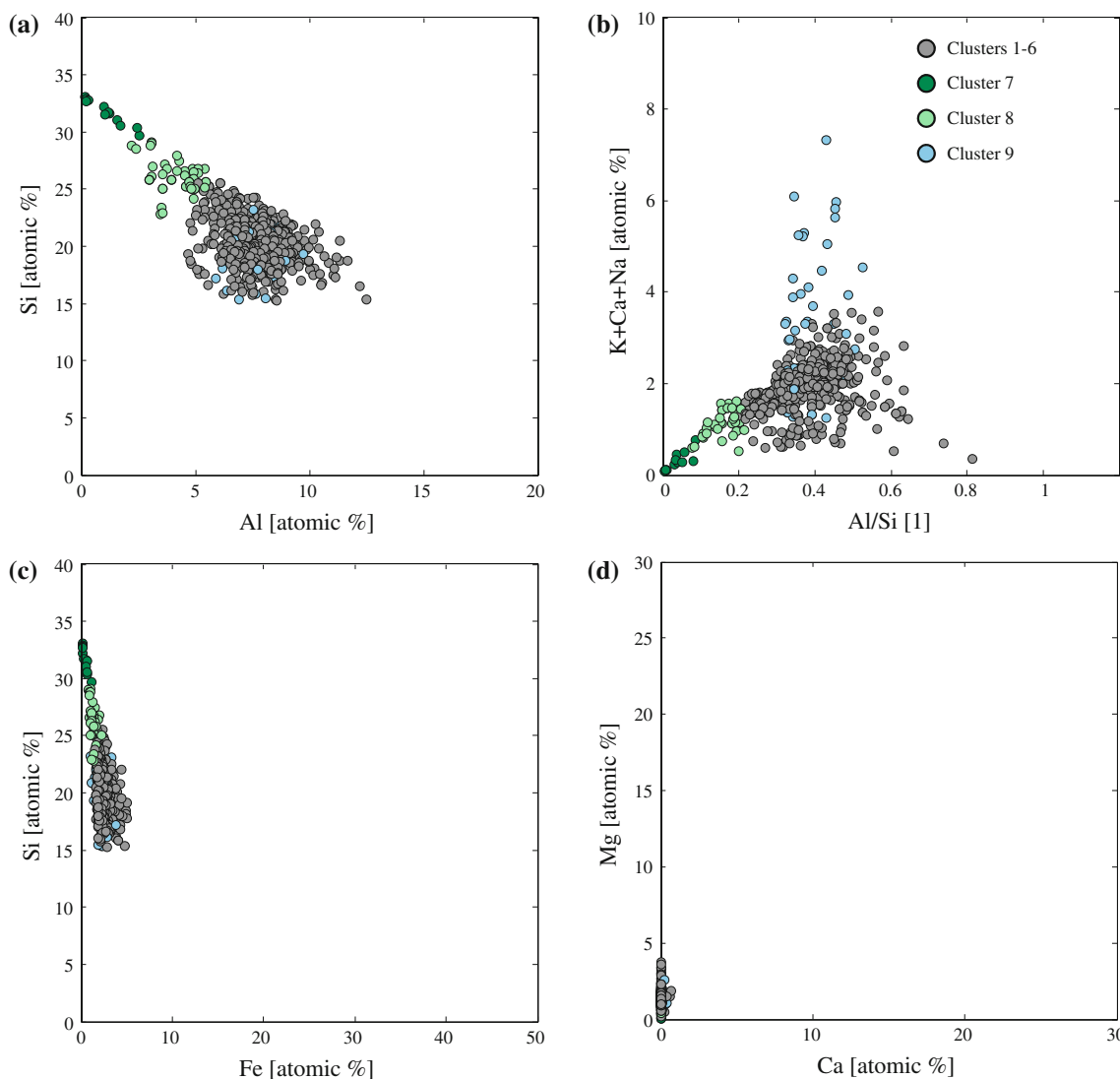


Fig. 5 Multi-variate cluster analysis of grid WDS data for experiment S3-W1. The nine phases identified through cluster modeling are displayed on 2-D projections of elemental atomic percentages. **a** Al-Si space. **b** Al/Si – K + Ca + Na space. **c** Fe-Si space. **d** Ca-Mg space

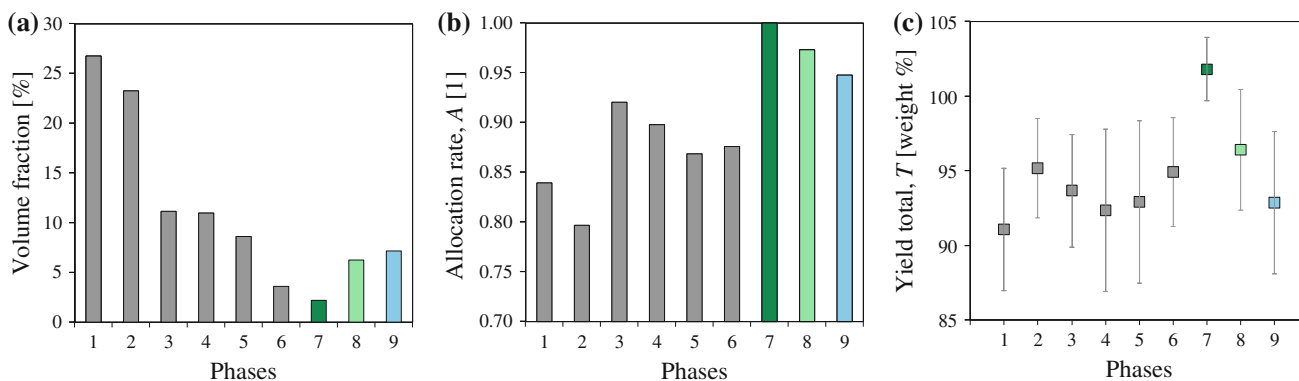


Fig. 6 Graphical representation of clustering statistics for experiment S3-W1 listed in Table 6. **a** Volume fractions, **b** allocation rates, and **c** yield totals

Table 6 Summary of the mean chemical properties, volume fractions V_i , allocation rates A_i , and yield totals T_i for the components identified by cluster modeling for experiment S3–W1

Phase, i	1	2	3	4	5	6	7	8	9
Si_i^μ [%]	19.27	21.08	18.68	21.99	19.68	21.39	31.64	26.24	19.53
Si_i^σ [%]	1.42	1.33	1.64	1.99	2.44	1.82	1.10	1.57	2.09
Al_i^μ [%]	7.74	7.84	8.14	6.15	8.89	7.52	1.16	4.12	7.58
Al_i^σ [%]	0.79	0.89	1.09	0.87	1.85	1.13	0.80	0.89	0.82
K_i^μ [%]	1.46	1.27	1.36	1.14	1.19	1.35	0.15	0.72	1.32
K_i^σ [%]	0.18	0.52	0.58	0.17	0.70	0.45	0.14	0.24	1.04
Ca_i^μ [%]	0.02	0.02	0.02	0.02	0.01	0.16	0.01	0.01	0.05
Ca_i^σ [%]	0.01	0.01	0.01	0.01	0.01	0.19	0.01	0.01	0.09
Na_i^μ [%]	0.76	0.56	0.60	0.53	0.43	0.39	0.14	0.39	2.16
Na_i^σ [%]	0.25	0.11	0.18	0.13	0.13	0.20	0.07	0.15	1.28
Fe_i^μ [%]	2.48	2.37	3.58	1.89	2.21	2.53	0.46	1.32	2.34
Fe_i^σ [%]	0.35	0.26	0.67	0.15	0.37	0.35	0.30	0.32	0.73
Mg_i^μ [%]	1.52	1.32	2.10	1.12	1.22	1.12	0.22	0.76	1.31
Mg_i^σ [%]	0.25	0.14	0.59	0.18	0.30	0.46	0.14	0.16	0.42
V_i [%]	26.8	23.3	11.1	11.0	8.6	3.6	2.2	6.3	7.2
A_i [1]	0.84	0.80	0.92	0.90	0.87	0.88	1.00	0.97	0.95
T_i^μ [%]	91.1	95.2	93.7	92.3	92.9	94.9	101.8	96.4	92.9
T_i^σ [%]	4.1	3.3	3.8	5.4	5.4	3.6	2.1	4.0	4.8

The variables μ and σ correspond to the mean and standard deviation of the given property

the feldspar site and clay components (Fig. 5b). No ligands were identified for hematite nor carbonate minerals. The small presence of these minerals as assessed by XRD (see Table 3) cannot be captured by the statistical WDS technique, which may require larger datasets to adequately sample the shale material for enhanced accuracy. The yield total statistics for ligand components follow those of clay components, attesting to the presence of clay in the probed microvolumes. Finally, the high values of allocation rates for quartz and feldspar mixtures underline the specific chemistries of the mixtures (i.e. considerable amounts of Si and K + Ca + Na, respectively), which enable the clustering algorithm to identify these components with high probabilities.

Similar implementations of the statistical WDS analysis were pursued for the remaining grids in our experimental program. Tables 7, 8 and 9 summarize their results in terms of mean chemical properties, volume fractions, allocation rates, and yield totals. In the following sections, the information generated by the statistical WDS method will be combined with grid indentation results to describe the chemomechanical signature of shale at micrometer scales.

5 Discussion

The following sections focus on synthesizing the results of grid indentation and WDS experiments. We first present

the interpretation of the indentation properties of shale based on purely mechanical considerations. This analysis is then complemented with the results from statistical WDS to provide precise definitions to the mechanically active phases in shale based on their chemical properties, with particular emphases on the porous clay in situ behavior and its response near boundaries of silt-size quartz and feldspar minerals.

5.1 Nanomechanics of shale from indentation considerations

The interpretation of cluster modeling results for grid indentations is pursued in this section solely on mechanics arguments. This approach, previously followed by [6, 56], brings together elements of the mechanical behaviors of shale constituents, length scale considerations, and overall material compositions known a priori from mineralogy tests to evaluate the grain-scale mechanics of shale.

Using as reference the experiments performed on shale S3, consistent indentation modulus and hardness (M , H) signatures were identified through cluster modeling (see Table 5). Three main types of mechanically active components were established, whose on-average properties are graphically compiled in Fig. 7. The first type corresponds consistently to the phase with large M , H values, whose response is expected due to the presence of quartz and feldspar inclusions. In Fig. 7a, b, the so-called

Table 7 Summary of the mean chemical properties, volume fractions V_i , allocation rates A_i , and yield totals T_i for the components identified by cluster modeling for experiment S3–W2

Phase, i	1	2	3	4	5	6	7	8	9
Si_i^μ [%]	19.32	19.54	19.56	19.96	21.40	21.53	22.49	23.54	27.35
Si_i^σ [%]	1.34	1.08	1.75	13.11	1.32	0.89	0.49	1.15	1.45
Al_i^μ [%]	8.10	8.78	8.58	8.30	8.10	7.58	6.43	6.05	3.11
Al_i^σ [%]	0.82	0.66	1.06	7.97	0.80	0.54	0.30	0.70	0.88
K_i^μ [%]	1.51	1.71	1.54	1.44	1.52	1.41	1.27	1.16	0.60
K_i^σ [%]	0.34	0.28	0.45	3.35	0.34	0.23	0.12	0.29	0.37
Ca_i^μ [%]	0.00	0.00	0.00	0.10	0.02	0.00	0.00	0.00	0.00
Ca_i^σ [%]	0.00	0.00	0.00	0.03	0.00	0.00	0.00	0.00	0.00
Na_i^μ [%]	4.05	1.47	1.55	1.96	1.45	1.18	0.91	0.98	0.56
Na_i^σ [%]	0.71	0.57	0.92	6.92	0.69	0.47	0.26	0.61	0.76
Fe_i^μ [%]	2.23	2.14	2.83	2.06	2.34	2.03	1.67	1.72	0.90
Fe_i^σ [%]	0.44	0.35	0.57	4.29	0.43	0.29	0.16	0.38	0.47
Mg_i^μ [%]	1.23	1.31	1.52	1.23	1.29	1.18	1.04	1.00	0.58
Mg_i^σ [%]	0.25	0.20	0.32	2.41	0.24	0.16	0.09	0.21	0.27
V_i [%]	8.4	30.5	17.2	2.5	3.4	21.7	3.3	7.9	5.0
A_i [1]	0.90	0.87	0.88	1.00	0.93	0.88	0.87	0.96	1.00
T_i^μ [%]	100.7	100.4	99.2	100.1	96.0	100.2	103.4	101.6	105.2
T_i^σ [%]	4.7	3.8	6.0	6.1	5.0	3.7	3.2	5.2	4.7

The variables μ and σ correspond to the mean and standard deviation of the given property

Table 8 Summary of the mean chemical properties, volume fractions V_i , allocation rates A_i , and yield totals T_i for the components identified by cluster modeling for experiment S3–W3

Phase, i	1	2	3	4	5	6	7	8	9	10
Si_i^μ [%]	18.50	19.71	19.73	20.52	24.52	30.33	20.26	22.63	22.99	22.84
Si_i^σ [%]	2.80	1.65	2.03	3.39	1.21	1.10	1.92	0.35	0.27	0.44
Al_i^μ [%]	9.25	7.88	7.88	7.54	5.00	1.55	7.92	7.61	7.66	7.53
Al_i^σ [%]	1.40	1.01	1.63	0.74	1.15	0.78	0.77	0.15	0.15	0.24
K_i^μ [%]	2.10	1.60	1.39	2.59	0.97	0.29	1.36	0.05	0.06	3.69
K_i^σ [%]	0.89	0.29	0.28	3.44	0.25	0.18	0.52	0.05	0.05	0.16
Ca_i^μ [%]	0.02	0.02	0.03	0.28	0.02	0.01	0.03	0.02	0.00	0.07
Ca_i^σ [%]	0.03	0.02	0.02	0.53	0.02	0.02	0.03	0.04	0.01	0.01
Na_i^μ [%]	0.82	0.69	0.76	1.81	0.52	0.20	2.82	6.56	6.03	3.83
Na_i^σ [%]	0.59	0.19	0.35	2.48	0.30	0.19	1.72	0.62	0.43	0.27
Fe_i^μ [%]	2.56	2.08	2.02	1.21	1.27	0.40	1.39	0.28	0.10	0.13
Fe_i^σ [%]	1.64	0.37	0.41	1.57	0.35	0.30	0.75	0.16	0.05	0.05
Mg_i^μ [%]	1.46	1.28	1.02	0.66	0.73	0.21	0.82	0.03	0.01	0.01
Mg_i^σ [%]	0.76	0.24	0.24	0.82	0.19	0.15	0.48	0.06	0.03	0.03
V_i [%]	7.1	29.3	13.3	3.1	6.7	3.2	8.8	2.1	18.3	8.1
A_i [1]	0.94	0.91	0.85	0.98	0.95	0.99	0.93	0.96	0.99	1.00
T_i^μ [%]	93.5	91.8	91.1	94.0	94.2	98.3	93.9	98.2	98.1	99.5
T_i^σ [%]	3.0	3.5	4.1	5.9	3.6	3.5	4.9	1.7	1.2	1.0

The variables μ and σ correspond to the mean and standard deviation of the given property

inclusion (INC) component type exhibits on-average indentation modulus and hardness values of approximately $M^{\text{INC}} \approx 80\text{--}110$ GPa, $H^{\text{INC}} \approx 11\text{--}18$ GPa. These observations relate in first order to the properties of quartz

($M = 80\text{--}100$ GPa, $H = 12\text{--}14$ GPa, [9, 24, 25]) and feldspar ($M = 89$, $H = 7$ GPa [64]). The large spread in data measured for the INC components can be attributed to the different types of occurrences of quartz and feldspar in

Table 9 Summary of the mean chemical properties, volume fractions V_i , allocation rates A_i , and yield totals T_i for the components identified by cluster modeling for experiment S7–W1

Phase, i	1	2	3	4	5	6	7	8	9	10
Si_i^μ [%]	15.47	15.48	15.74	16.64	16.66	18.64	30.91	33.23	23.93	18.35
Si_i^σ [%]	1.06	1.68	3.91	1.12	1.29	0.90	1.04	0.13	0.97	3.45
Al_i^μ [%]	11.86	11.29	9.77	11.77	11.19	10.84	0.66	0.01	4.43	9.73
Al_i^σ [%]	1.44	1.44	2.27	0.84	1.45	2.04	0.49	0.06	1.62	0.76
K_i^μ [%]	0.51	0.51	0.51	0.51	0.82	0.54	0.06	0.00	0.26	2.29
K_i^σ [%]	0.26	0.14	0.22	0.07	0.30	0.14	0.13	0.01	0.12	1.99
Ca_i^μ [%]	0.14	0.12	0.35	0.05	0.06	0.08	0.01	0.00	0.03	0.13
Ca_i^σ [%]	0.11	0.09	0.33	0.03	0.04	0.05	0.03	0.00	0.05	0.20
Na_i^μ [%]	0.53	0.54	0.46	0.54	0.40	0.29	0.04	0.00	0.23	1.05
Na_i^σ [%]	0.23	0.21	0.24	0.24	0.12	0.19	0.05	0.01	0.25	1.32
Fe_i^μ [%]	2.56	1.74	3.58	1.23	1.30	1.42	0.16	0.05	0.60	0.87
Fe_i^σ [%]	1.32	0.78	2.76	0.13	0.26	0.44	0.18	0.03	0.28	0.43
Mg_i^μ [%]	0.65	0.49	0.74	0.46	0.49	0.36	0.04	0.00	0.20	0.30
Mg_i^σ [%]	0.33	0.14	0.53	0.07	0.12	0.21	0.07	0.01	0.11	0.22
V_i [%]	3.8	12.9	9.0	21.7	10.6	8.1	7.5	18.8	2.3	5.3
A_i [1]	0.96	0.91	0.98	0.93	0.94	0.95	1.00	1.00	1.00	1.00
T_i^μ [%]	88.8	85.7	88.2	88.4	87.8	91.5	96.2	100.7	88.5	90.3
T_i^σ [%]	3.1	5.0	8.8	4.1	4.6	4.5	4.6	1.3	6.6	7.3

The variables μ and σ correspond to the mean and standard deviation of the given property

shale. Quartz grains are often of detrital nature and can occur as either single or polycrystalline grains. If in polycrystal form, the expected mechanical properties of quartz would be lower compared to behaviors of single grains given then presence of weak grain boundaries. In addition, the indentation experiments associated with stiff (hard) INCs exhibited indentation depths ($h_{\text{max}}^{\text{INC}} \approx 160\text{--}220$ nm) that are close to the RMS roughness of the material sample. The comparable length scales of indentation depths and surface roughness may affect the extraction of modulus and hardness values from the load-deformation responses. The second type of mechanical response corresponds to the components with lower M , H values compared to INCs and with low volume fractions (<30 %, Fig. 7c). These so-called composite (COMP) phases also exhibit low allocation rates. Finally, the third type of mechanical component corresponds to the porous clay (PC) phase, identified by the notoriously large volume fraction (Fig. 7c) as expected from e.g. XRD mineralogy assessments. The PC phase type is consistently identified with high allocation rates (Fig. 7d), and exhibits the lowest M , H values compared to the INC and COMP components. The load-deformation response shown in Fig. 4c for the experiment clustered in component 1 (the porous clay phase) represents the mechanical response expected qualitatively for a clay medium, with significant plasticity and creep behaviors (see also [67]). Consolidating the understanding of the PC

phase from indentation considerations also requires an evaluation of the length scales associated with the indentation experiments. With average maximum indentation depths of approximate $h_{\text{max}}^{\text{PC}} \approx 800$ nm, the interaction volumes in indentation experiments associated with the PC phase access a length scale in shale which encompasses the clay minerals and the nanoporosity.

The stiffness and hardness properties of the mechanical PC phase inferred from cluster modeling are fairly consistent for the different grid experiments. Figure 8 displays the mean values and standard deviations for the indentation modulus and hardness of the PC phase in the four experiments covered in our experimental program. The results of Bobko and Ulm [6] for shale S3 and S7 sister samples reanalyzed using the EM–ML clustering method [47] are presented in the figure. The indentation modulus and hardness properties compare adequately across the different experiments, supporting to the robustness of the statistical indentation technique applied to shale. The mechanically active components in shale at the micrometer scale appear to be identified reliably and consistently from grid indentation experiments. However, two questions remain about these indentation assessments. Is the mechanical behavior of the PC as inferred by statistical indentation associated with the clay fabric of shale from a strict chemical standpoint? Furthermore, what is the chemical nature of the so-called mechanical COMP

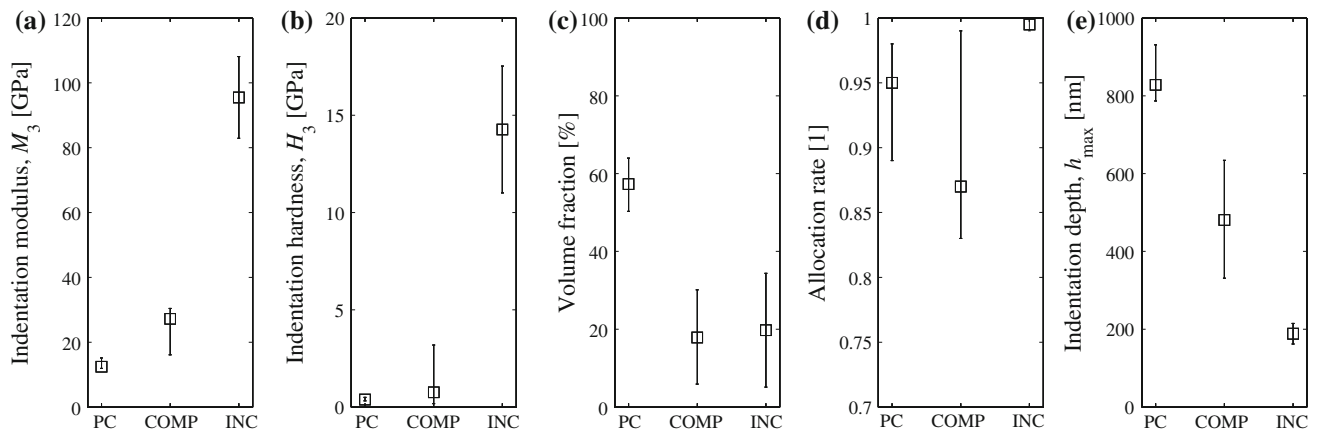


Fig. 7 Compilation of cluster modeling results for grid indentations on shale S3. Their interpretation establishes three mechanically active components: the porous clay (PC) component, the mechanical composite (COMP) components, and the inclusion (INC) component. Plots **a–e** display the on-average properties established for each component. The *solid data points* and *error bars* correspond to the median, maximum, and minimum (on-average) values, respectively, determined for experiments S3–I1, S3–I2, and S3–I3

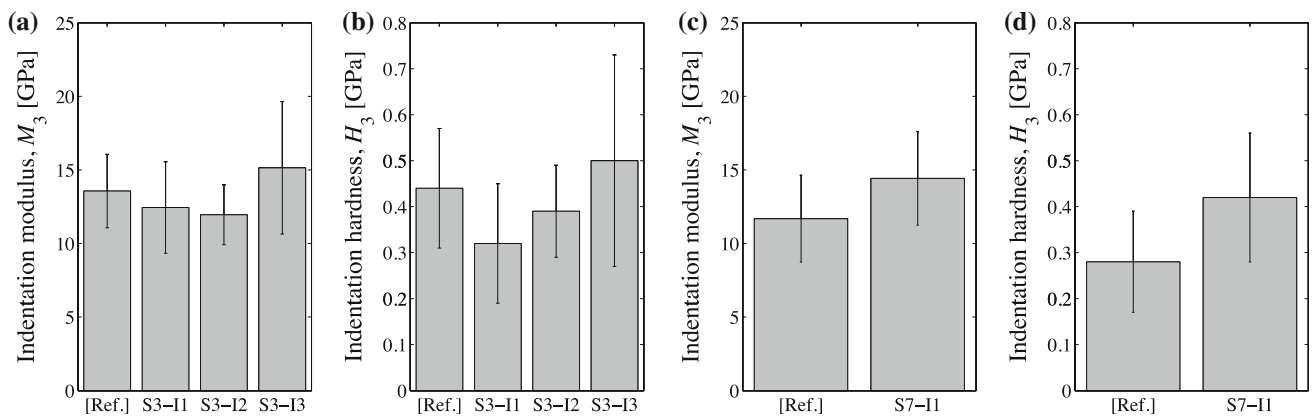


Fig. 8 Comparisons of modulus and hardness values for the porous clay phase in shales S3 and S7 inferred from cluster modeling of grid indentation experiments. The data are presented in terms of mean values, whereas the *bars* represent the associated standard deviations. Reference (Ref.) corresponds to the indentation data of Bobko and Ulm [6] reanalyzed using the EM–ML approach for cluster modeling. The experiments S3–I1, S3–I2, S3–I3, and S7–I1 were used for the comparisons

component identified by statistical indentation? These questions will be addressed in the two subsequent sections.

5.2 Coupled chemomechanical analysis of the porous clay

The cluster modeling results of grid WDS data in experiments S3–W1 and S3–W2 are employed to establish the chemical constitution of the PC mechanical phase inferred from statistical indentation. Figure 9 displays a series of maps of the grids of indentation and WDS experiments, in which each pixel corresponds to a local measurement within the resolution of the grid spacings. Figure 9a, d displays the data corresponding to the mechanical PC inferred from statistical indentation. The backgrounds in those figures represent the data associated with the remaining mechanical components (i.e., COMP and INC

phases), as well as data that were discarded from the analysis due to defective load–deformation curves. Similarly, Fig. 9b, e displays the data for the clay components defined by statistical WDS, and for which the backgrounds represent data associated with other chemical components (i.e., quartz, feldspar, quartz–clay mixture, etc.) and discarded data with low yield totals. The previous maps are employed to construct Fig. 9c, f. In each figure, the mechanical PC component is matched with the chemical clay components inferred for each sample surface. The resulting chemomechanical maps represent the set of indentation and WDS experiments that are associated simultaneously to mechanical and chemical clay components. The coupled grids in Fig. 9c, f show satisfactory matchings for the PC phases, with 85 % or more of the mechanical PC data being linked to the chemical data. The results presented in Fig. 9 formalize the conjecture about

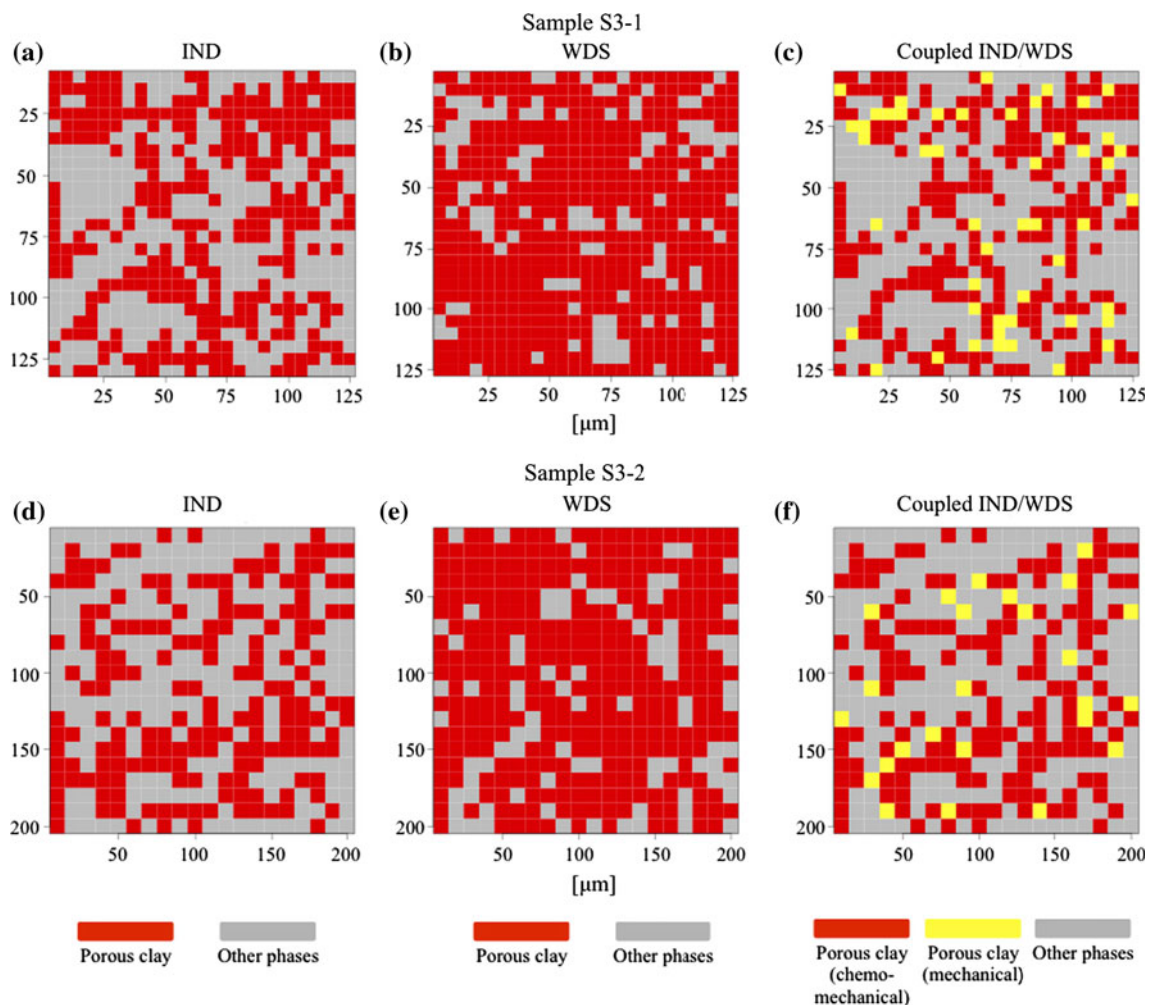


Fig. 9 Coupled indentation/WDS assessments of shale S3 identifying the porous clay chemomechanical component over locations S3-1 and S3-2. For each sample surface, the maps display the spatial distributions of the grid indentation (IND) and WDS data associated with **a, d** the porous clay mechanical component (cluster 1, Table 5), and **b, e** the clay chemical component (Tables 6, 7). **c, f** Display the overlap of the data presented in the indentation and WDS grids, establishing the chemomechanical porous clay inferred by the coupling of both analyses. The data for the mechanical porous clay **a, d** not matching the chemical assessment **b, e** are also displayed with a distinctive *color*. The discretization of the mechanical and chemical maps is related to the size of the spacing used in the indentation and WDS experiments (5 and 10 μm for grid experiments S3-1 and S3-2, respectively). Other phases refer to the remaining mechanical or chemical components identified by cluster modeling in addition to mechanical data discarded from indentation experiments and WDS data filtered due to low yield totals

the PC phase in shale at the scale of micrometers being related to the mechanical component with the largest volume fraction and lowest stiffness and hardness values probed by grid indentations. Our chemomechanical analysis shows that the mechanical PC sensed by nanoindentation indeed corresponds to clay material sensed by EPMA.

5.3 Coupled chemomechanical analysis of the composite phase

Separate studies were conducted to determine the mechanical and chemical natures of the so-called COMP phases inferred from indentation experiments on shale.

Two coupled grid indentation and WDS experiments were conducted on specific regions of shales S3 and S7 which contained sizable grains. These regions were also imaged using BSE and X-ray mapping techniques to obtain visual descriptions of the underlying microstructures (the actual order of experiments performed for surface S3-3 and S7-1 was: grid indentation, WDS analysis, and BSE/X-ray mapping). The imaging information provides the baseline for linking the spatial configuration of the material structure to the results of coupled indentation and WDS grids. The BSE and X-ray maps presented in Figs. 10 and 11 show the microstructures associated with experiments S3-3 and S7-1, in which large INCs of approximately 100 μm in characteristic size are clearly visible. The sampled

regions are approximately between 150×150 and $250 \times 250 \mu\text{m}^2$, respectively. Five elements were selected for X-ray mapping (Si, Al, Fe, K, Na), which can be used to qualitatively identify the major INCs present on the probed surface. In experiment S3-3, the large grain is recognized as feldspar, in accord with the moderate concentrations of silicon and aluminum and high concentrations of potassium and sodium. The concentrations of these elements result in two characteristic regions visible within the grain. Several smaller quartz grains are also identified by high concentrations of silicon and the absence of other elements. The remaining portions of the surface are related to the fine-grained matrix of clay minerals. Similarly, the analysis of images for experiment S7-1 shown in Fig. 11 reveals the presence of several sizable quartz grains given the high contrast between silicon and aluminum maps. The remaining portions of the surface are related to the clay matrix and small grains of feldspar and quartz.

The surfaces detailed in Figs. 10 and 11 were used for coupled grid indentation and WDS experiments. Following similar analyses to those described in Section 4, the results of cluster modeling for experiments S3–W3/S3–I3 and S7–W1/S7–I1 are graphically gathered in Figs. 12 and 13. The cluster modeling for grid WDS experiments (Figs. 12a,

13a) recognizes the presence of clay, quartz, and feldspar components (poles), as well as mixtures of quartz-clay and feldspar-clay (ligands) within the probed microvolumes. The compilations of these results are displayed spatially over the actual grids of measurements in Figs. 12c and 13c. The chemical components identified through cluster modeling provide remarkable descriptions of the local chemistries in the material surfaces. The COMP grain of feldspar (Fig. 12c) is well defined using the information from clusters 7–10. The clay matrix associated with clusters 1–4 surrounds the large feldspar INC and the small regions of quartz INCs related to clusters 5 and 6. The sizable grain of quartz (Fig. 13c) is well captured through clusters 7–9, and the clay matrix and small feldspar grains associated with clusters 1 through 6 and 10, respectively, are also clearly identified. The analysis of the third battery of tests consisting of grid indentations is presented in Figs. 12b and 13b. In both cases, cluster 1 corresponds to the PC mechanical phase, with mechanical properties in good agreement with other grid indentation results (see Fig. 8). This adequate comparison justifies the selected grid spacings of 5 and 10 μm required to achieve spatial resolution without causing mechanical interactions between the deformed microvolumes in indentation experiments. The

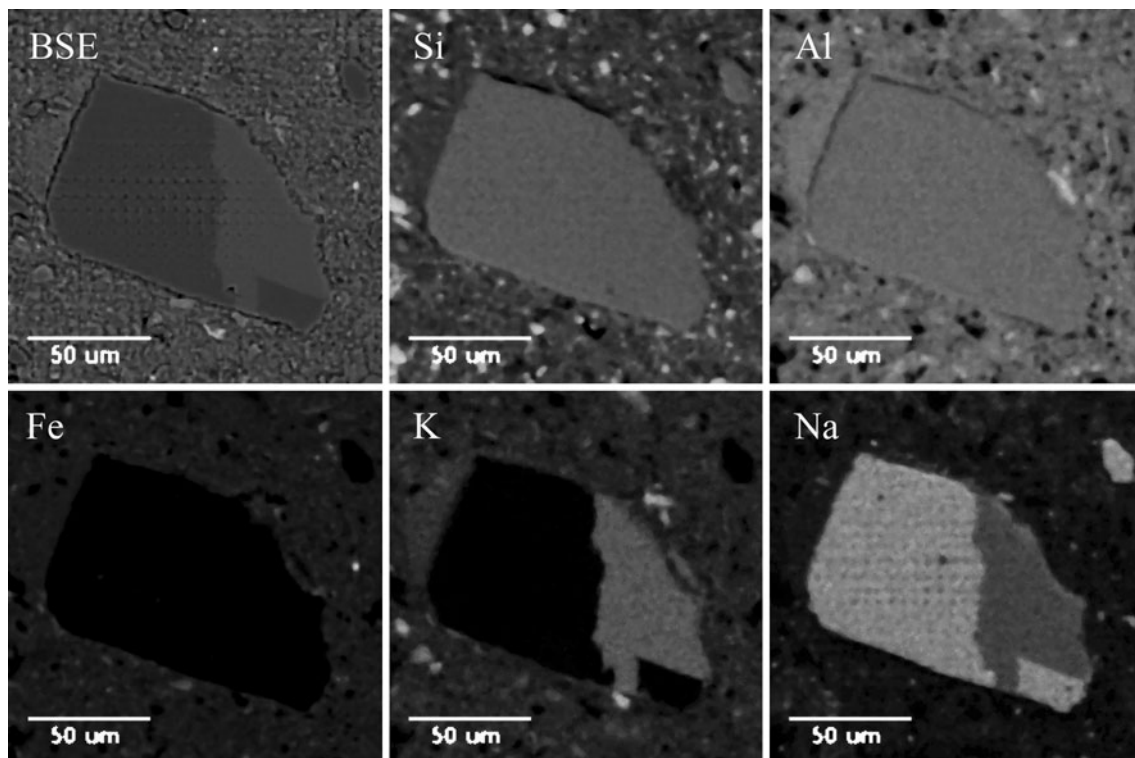


Fig. 10 BSE and X-ray imaging of experiment S3-3. The particular spot for these EPMA experiments was chosen deliberately as it contains a sizable feldspar grain. The five X-ray maps display the relative amounts of the particular elements in the material surface, and the dark-to-light transition corresponds to a low-to-high concentration gradient. The analysis of the X-ray maps characterize the inclusion as feldspar. The matrix surrounding the inclusion contains clay minerals and some small quartz grains

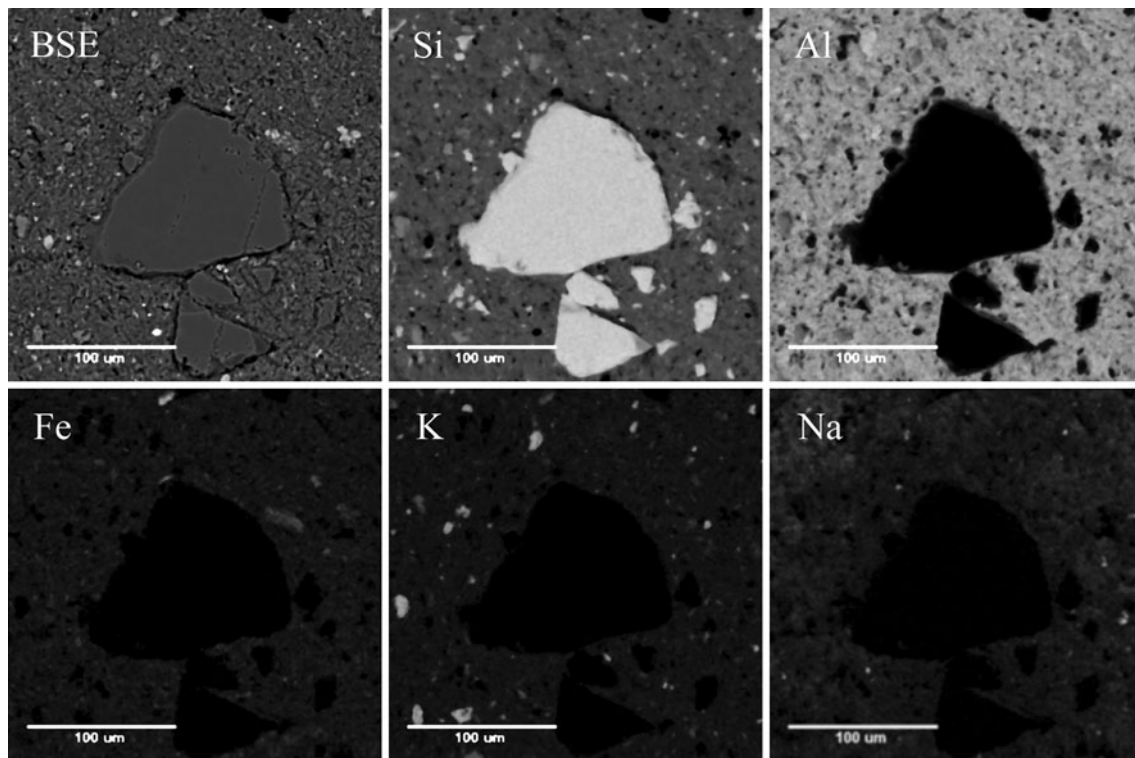


Fig. 11 BSE and X-ray imaging of experiment S7-1. The particular spot for these EPMA experiments was chosen deliberately as it contains several sizable quartz grains. The five X-ray maps display the relative amounts of the particular elements in the material surface, and the dark-to-light transition corresponds to a low-to-high concentration gradient. The analysis of the X-ray maps characterize the major inclusions as quartz. The matrix surrounding the inclusions contains clay minerals and some small quartz and feldspar grains

phases associated with COMP responses (cluster 2 in Fig. 12b, and clusters 2 and 3 in Fig. 13b) and INCs (clusters 3 and 4 in Figs. 12b, 13b, respectively) are properly identified. The results from cluster modeling are also displayed Figs. 12d and 13d, showing the spatial arrangements of each set of grid indentations. The feldspar grain in Fig. 12d is delineated by data points from cluster 3. While these data exhibit large modulus and hardness values, the range of INC properties is above expected values for feldspar grain (Sect. 5.1). This mismatch in properties could be related to the shallow indentation depths for these experiments in relation to the roughness of grain, which could also explain the failure to retrieve some of the indentation data within the region of the grain itself. Nevertheless, the grain boundary appears to be well delimited by the indentation data related to cluster 3. The spatial representation of grid experiments in Fig. 13d captures the large quartz grains within this shale surface.

The experimental evidence presented here offers the necessary elements to discern the nature of the so-called COMP mechanical phases. Given the adequate delineation of the feldspar grain as observed in Fig. 12d, the data for the COMP mechanical component (cluster 2) is related mainly to the surroundings of the feldspar grain. Other data linked to the mechanical COMP component are situated in

other locations of the material surface, which are related to the proximities to small quartz grains. Similar observations are made for the mechanical COMP components (clusters 2 and 3) in Fig. 13d, whose data surround the sizable quartz grains and bridges to the mechanical PC component. The coupled chemomechanical results reveal that the fractions of data encompassed in the mechanical COMP components correspond to the chemical clay phase inferred from WDS cluster modeling. These results properly establish the mechanical COMP components found in grid indentations on shale as tests performed on conglomerates of clay particles near stiffer (harder) INCs of quartz or feldspar. This local mechanical behavior measured by nanoindentation is truly a COMP response, in which the low indentation properties of the clay fabric are altered by the presence of nearby rigid-like grains. In contrast, measurements away from boundaries with quartz and feldspar grains provide consistent mechanical measurements that characterize the PC phase of shale.

5.4 Nanomechanics modeling of shale

The PC mechanical phase of shale has been properly identified by the proposed coupled indentation and WDS methodology. Its chemomechanical signature represents

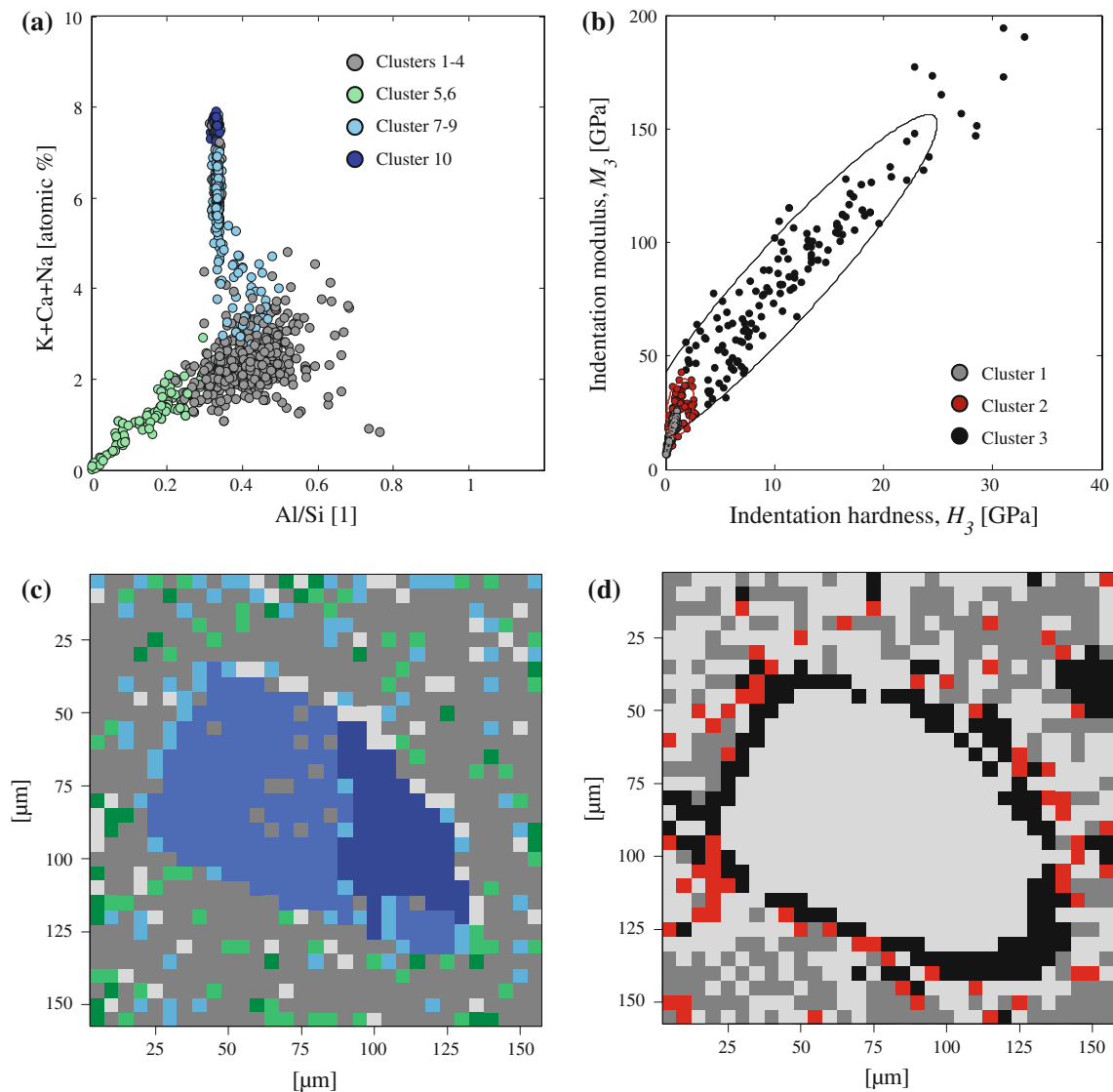


Fig. 12 Cluster modeling of **a** grid WDS and **b** grid indentation data for the surface S3-3. The coupled experiments were performed over the same location of the EPMA imaging studies (S3–X3) presented in Fig. 10. The interpretation of statistical clustering of WDS data recognizes four types of chemical constituents associated with clay (clusters 1–4), quartz-clay mixtures (clusters 5, 6), sodium-rich feldspar (clusters 7–9), and potassium-rich feldspar (cluster 10). The interpretation of statistical clustering of indentation data recognizes the characteristic three types of mechanical responses: porous clay (cluster 1), composite (cluster 2), and inclusion (cluster 3). **c** and **d** Display the clustering results of the grid WDS and indentation experiments in their spatial distributions over the probed surface

the response of the clay matrix away from silt INCs such as quartz and feldspar. Furthermore, the nanomechanics of the PC can be described statistically in terms of mean stiffness and hardness properties for the particular shale material. To broaden the far reaching implications of our experimental findings, we revisit the database compiled by Bobko and Ulm [6] to establish connections between measured nanomechanics and composition of several shale materials. This database, which includes sister samples of shales S3 and S7, covers a broad spectrum of compositional properties for shales. The grid indentation data developed in [6] were reanalyzed in [44, 47] using the ML–EM clustering

method (e.g. see Fig. 8). The statistical clustering treatment recognized consistently the porous clay, COMP, and INC components for experiments in the normal and parallel-to-bedding directions on all shale samples considered in the study. The indentation properties of the porous clay component, which is formalized in this study as the chemo-mechanical phase composed of clay and nanoporosity and located away from silt INCs, compared adequately with the modulus and hardness values obtained by the deconvolution analysis of Bobko and Ulm [6]. To show the range of compositions, Fig. 14a displays the overall volume fraction makeup for each of the shale materials considered in the

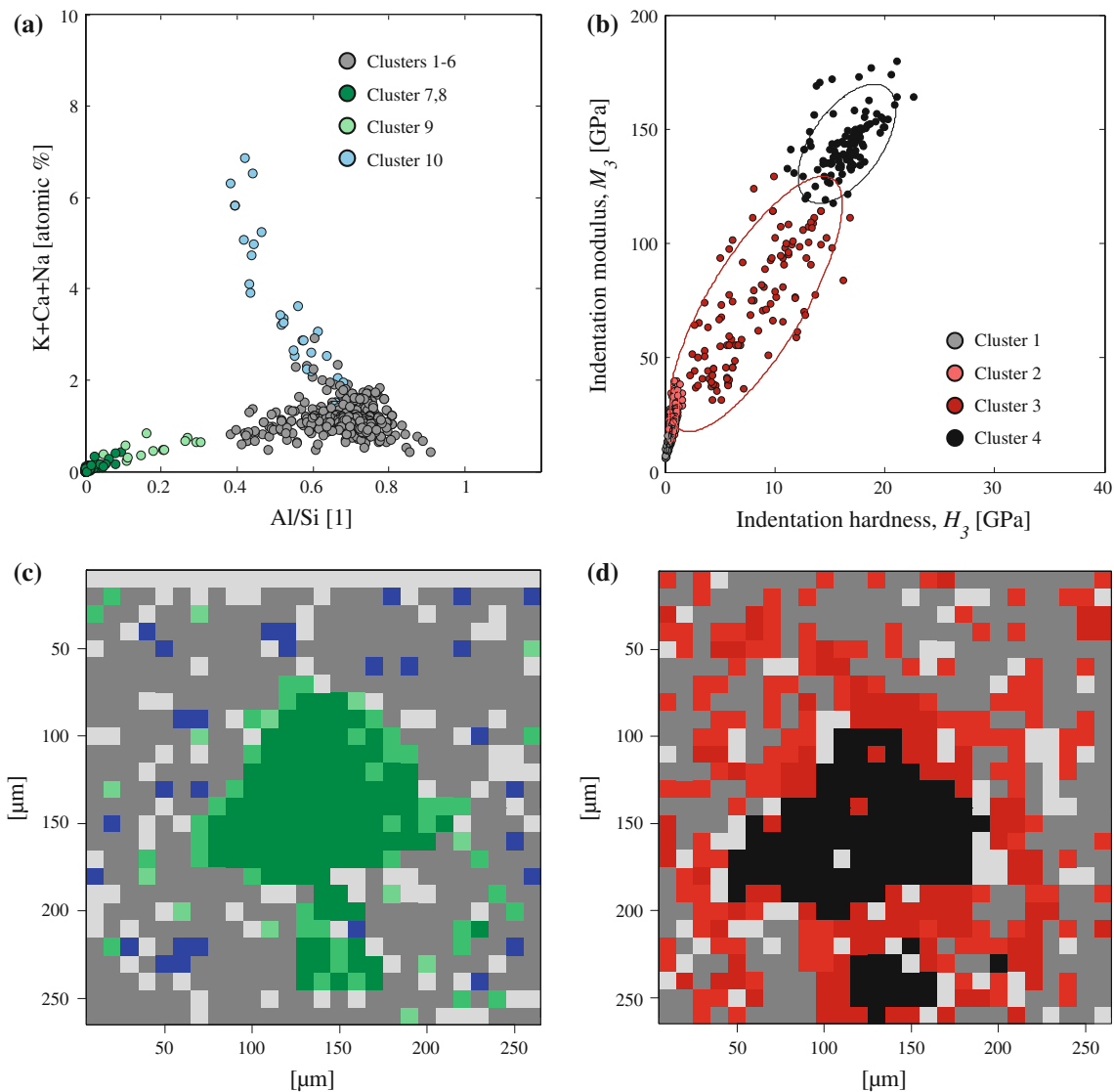


Fig. 13 Cluster modeling of **a** grid WDS and **b** grid indentation data for the surface S7-1. The coupled experiments were performed over the same location for the EPMA imaging studies (S7–X1) presented in Fig. 11. The interpretation of statistical clustering of WDS data recognizes four types of chemical constituents associated with clay (clusters 1–6), quartz (clusters 7, 8), quartz-clay mixture (clusters 9), feldspar-clay mixture (cluster 10). The interpretation of statistical clustering of indentation data recognizes the characteristic three types of mechanical responses: porous clay (cluster 1), composites (cluster 2, 3), and inclusion (cluster 4). **c** and **d** Display the clustering results of the grid WDS and indentation experiments in their spatial distributions over the probed surface

database. The volume fraction contribution for each mineral constituent was calculated as described in (8), which implements XRD mineralogy and MIP porosity data for the calculation. The data are displayed in terms of partial volume fractions associated with silt INCs (quartz, feldspar and others), 2:1 clays (mainly illite and smectite), kaolinite, and other clays. The contribution from the porosity measured by MIP experiments is also included in the overall volume. The inspection of Fig. 14a reveals a diverse compositional makeup for the different shale materials, especially varying amounts of clay minerals: for example, shales S3, S4, and the Pierre shale are 2:1 clay dominated,

whereas shale S7 and the Dark shale exhibit similar volume fractions of 1:1 and 2:1 clays.

The compositional descriptions of the seven shales in Fig. 14a are compared to the statistical indentation results presented in Fig. 14b. With the focus on elasticity, the figure displays the means and standard deviations of the two measured indentation moduli associated with the PC phases of each shale material. The indentation M_1 corresponds to the experiment performed parallel to the natural bedding planes observed in the bulk shale sample, whereas M_3 corresponds to the normal to bedding direction (which is the direction for all our experiments reported in Table 5).

The indentation data are arranged as a function of the clay packing density, which neatly synthesizes the composition and porosity information into one parameter. Considering the overall macroscopic composition of shale (level II) as the total contributions of clay f^{clay} , silt INCs f^{inc} , and porosity ϕ volume fractions, the clay packing density is defined as:

$$\eta = \frac{f^{\text{clay}}}{1 - f^{\text{inc}}} = 1 - \frac{\phi}{1 - f^{\text{inc}}} \quad (9)$$

The clay packing density (or alternatively, the nanoporosity $\phi = 1 - \eta$) becomes the scaling parameter for the mechanical response of the PC COMP (level I), as it normalizes the volumetric contributions of the clay and porosity by the silt INC material present in the shale sample. Each solid data point in Fig. 14b corresponds to the mean clay packing density estimated from two different assessments of porosity (directly measured through MIP or inferred from density values) and mean indentation

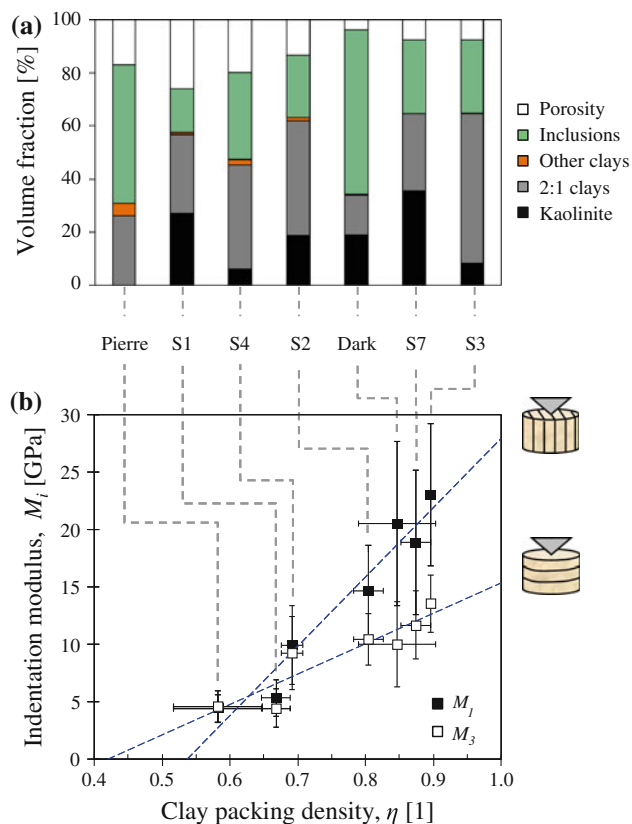


Fig. 14 **a** Compositions of seven shale materials given in volume fractions of kaolinite, 2:1 clays (illite–smectite), other clays, silt inclusions (quartz, feldspar), and porosity (measured by MIP experiments). **b** Porous clay stiffness and clay packing density values for shale materials in **a**. The stiffness corresponds to the indentation moduli inferred from cluster modeling of grid indentation data. Indentation experiments were performed in the parallel to bedding (M_1) and normal to bedding (M_3) directions. Linear regressions are included to emphasize the experimental trends

modulus (M_1^u or M_3^u) obtained from cluster modeling of grid indentation experiments. The anisotropic indentation moduli and clay packing density display a remarkable global trend where increasing modulus values correspond to increasing packing densities. A solid percolation threshold exists at packing densities near $\eta \approx 0.5$ following this trend toward small modulus values. The apparent percolation threshold suggests a nanogranular behavior for the PC COMP, and can be related to microstructural features of the clay fabric such as particle orientations and shapes [47]. The mechanics of the PC for the asymptotic case of $\eta \rightarrow 1$ implies the response of an effective solid clay that is anisotropic and that displays elasticities well below those reported for single clay minerals (with $M_1 > M_3 > 46$ GPa, see review in [7]). The order of magnitude for the inferred in situ clay response agrees with previous experimental and modeling studies. Prasad et al. [48] measured an elastic modulus for dickite, which atomic structure closely resembles that of kaolinite, of 6.2 GPa using AFM testing. Bathija et al. [4] measured indentation moduli for two montmorillonite samples between 4 and 14 GPa. Katti et al. [30] conducted atomistic simulations on pyrophyllite, a precursor of other minerals in the smectite group. The derived elastic modulus of 13.2 GPa was attributed to the effect of interlayers in the clay unit. The in situ properties of solid clay at micrometer scales inferred from Fig. 14a represent the response of agglomerated clay units comprising the mechanical contributions of clay platelets, interlayer materials (absorbed water, hydrated cations) and interparticle contacts.

The scaling between indentation moduli and clay packing density emphasizes the effect of the nanoporosity as a main driver of the anisotropic elastic behavior of the PC in shale. This global trend between mean stiffness (M_i^u) and overall composition (consolidated in the η parameter) already reported in [6, 56] represents a new level of refinement in the poromechanics understanding of shale. The classical empirical relations at the macroscopic scale between modulus (e.g. acoustic velocities or Young's modulus) and the overall porosity are now complemented by the in situ nanomechanics of the porous clay shown in Fig. 14b. The analysis of the $M_i^u - \eta$ relationship and the overall compositional characteristics of each shale material in Fig. 14a establishes that the clay packing density controls the mechanics of the PC in shale at the microscales. Furthermore, the poor correlations between indentation response and clay mineralogy highlight the secondary role of the latter. As a result, the mechanical effects of different clay mineralogies, which contribute with different stiffness properties to the matrix, are modulated by the compliant natures of nanopores, interlayer materials, and interparticle contacts. This description is restricted to the elastic behavior of shale, as clay mineralogy is key to

describe other physical phenomena such as swelling and permeability.

Our coupled chemomechanical studies further enhance the descriptions of global trends for the in situ mechanics of the PC fabric. Figure 15a shows diagrammatically a data point presented in Fig. 14b. The mean indentation modulus (solid data point) is supplemented by the variability in modulus values estimated by the statistical cluster modeling (vertical bar covers two standard deviations). Using experiments S3–I1 and S7–I1 as illustration, Fig. 15b, c display the histograms of the indentation data measured for the PC in those experiments (clusters 1 in Figs. 4a, 13b, respectively) and the associated cluster modeling results (normal distributions with M_3^u , M_3^s properties defined in Table 5). The coupled chemomechanical information generated for these shale materials allows exploring the nature of the variation in mechanical properties captured in

the grid experiments. The grid WDS data associated with the clay matrix properties for experiments S3–W1 and S7–W1 (clusters 1–6 in Fig. 5b and clusters 1–6 in Fig. 13a, respectively) are replotted in Fig. 15d, e. In addition to the data of single WDS experiments, the mean chemical properties in the K + Ca + Na – Al/Si elemental space for the modeled clay clusters and the literature data for clays (see Fig. 2b) are also displayed in the figures. Qualitatively, the mean properties for the clay clusters are in good agreement with the clay mineralogies reported in XRD experiments (Table 2), in which 2:1 clays are dominant in shale S3 and similar proportions of 1:1 and 2:1 clays are found in shale 7. The relative proportions of these clay families for the latter sample are deduced from Fig. 15e through the positions of the clay clusters between the poles of 1:1 and 2:1 clays. These results from statistical WDS imply a solid mixture of these minerals at the scale of the

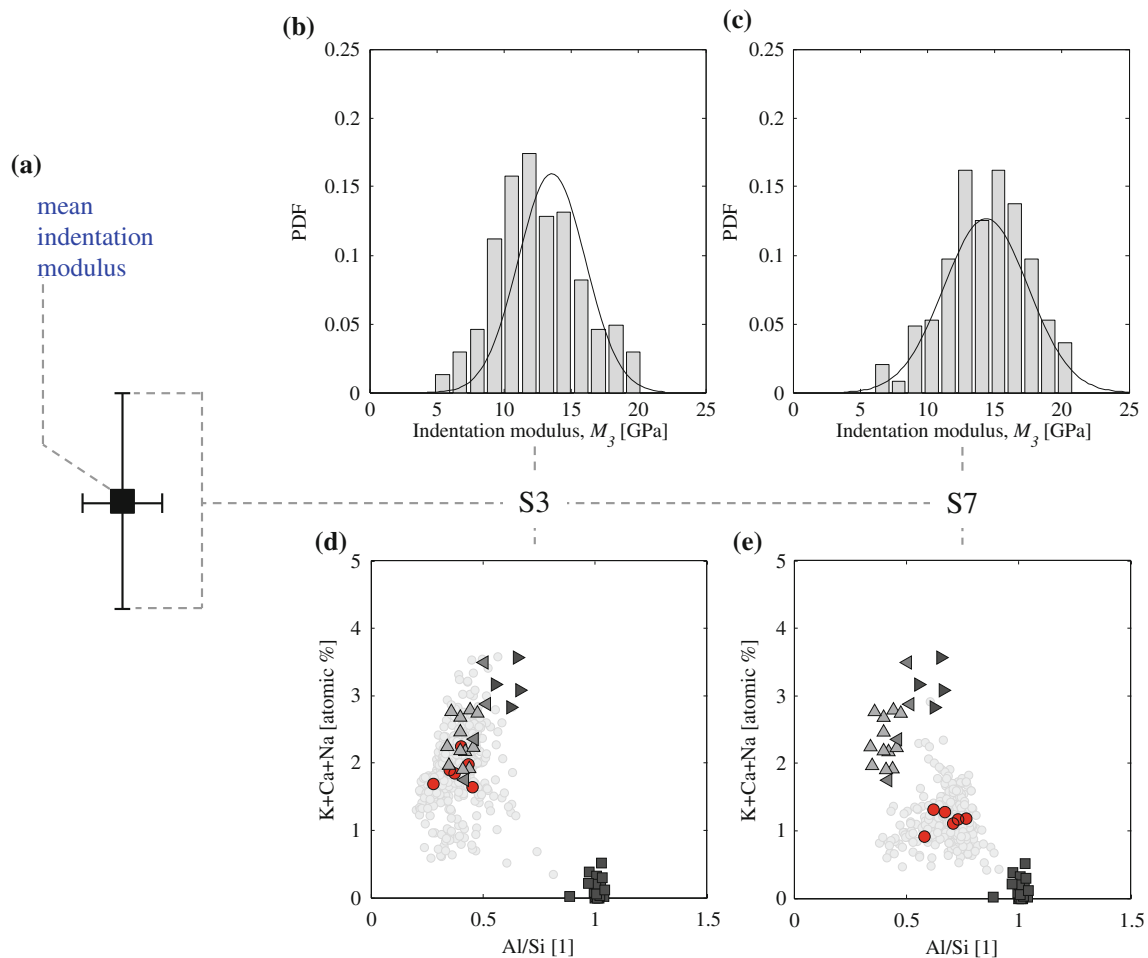


Fig. 15 Diagram of a data point presented in Fig. 14b showing the mean (solid point) and standard deviation (vertical bar) of the indentation modulus of the porous clay measured in grid experiments. **b** and **c** Indentation modulus M_3 data for shales S3 and S7 displayed in histograms. The accompanying normal distributions employ the cluster modeling results for clusters 1 in experiments S3–I1 and S7–I1 from Table 5. **d** and **e** Grid WDS data associated with clay components. Data in circles correspond to the mean chemical properties of the clay components identified through cluster modeling. Other data correspond to common compositions from the open literature of 1:1 and 2:1 clay mineralogies (see Fig. 2b)

WDS experiment of micrometer resolution. The novel information about compositions of shales S3 and S7 is the quantifiable variability of the chemistry of their clay matrices. A corollary of this observation is the potentially different local mechanical responses in the clay matrix due to different clay crystal elasticities. Another possible source of mechanical variability within the clay fabric in shale in addition to varying local chemistries is the presence of varying local porosities contained within the microvolumes probed in indentation experiments. In contrast to the chemical variability quantified in Fig. 15d, e, the variability in local porosities is only a postulate given the difficulty in measuring the void space of micrometer-sized material volumes experimentally. Having brought forward these two observations for the varying local mechanics of the PC phase, Fig. 16 displays the standard deviations of modulus values M_i^σ as functions of the clay packing density for the different shale materials covered in Fig. 14. The standard deviation values are normalized by the mean indentation modulus values M_i^μ to account for the different magnitudes of elasticity observed for the global trend $M_i^\mu - \eta$ in Fig. 14b. The analysis of Fig. 16 shows that the normalized standard deviation values fall within a narrow range between $M_i^\sigma/M_i^\mu = [0.2, 0.4]$ with no evident scaling with the clay packing density. Consequently, the local variabilities in clay chemistry observed in experiments S3–W1 and S7–W1 (Fig. 15d, e) do not dictate alone the mechanical signatures for the ranges of PC properties. In general, local variabilities in chemistry and porosity, which cannot be recapitulated separately at micrometer scales, may be at the source of the mechanical variations within the clay fabric response in shale. However, the overall stiffness captured by a mean indentation modulus is

controlled by the clay packing density representative of the particular shale material despite its clay composition.

6 Conclusions

The nanomechanics of shale quantified by statistical indentation has been strengthened in this work by an experimental investigation of its chemical makeup at similar length scales. The coupled chemomechanical analysis of grid indentation and WDS experiments confirmed that the PC mechanical phase in shale inferred by the statistical indentation method corresponds to the clay mineral phase defined strictly on chemical grounds. The PC characteristic stiffness and hardness behaviors are realized spatially in regions removed from silt INCs of quartz and feldspar. The higher mechanical properties of the silt INCs alter the mechanical behavior of the clay matrix near the grain boundaries. This COMP behavior sensed by indentation is captured by mechanical components inferred from cluster modeling which display modulus and hardness properties between those of the two bounding solids (i.e. the compliant PC and the stiff silt INCs). At the length scale of micrometers shared by both indentation and WDS experiments, there exists a chemo-mechanical signature for the PC that is consistent across shale materials with little organic matter. For the elastic behavior, the clay packing density (or alternatively the nanoporosity) modulates the on-average magnitude of the stiffness response of the porous clay fabric. The complex heterogeneous nature of this phase is observed in the local variabilities of indentation properties and chemistries, although these behaviors are of second order compared to the trends observed for mean mechanical properties and nanoporosity. The mechanical response of the PC phase determined by the statistical indentation technique becomes valuable experimental evidence for the benchmarking of multi-scale models for shale. In particular, the development of predictive theoretical schemes relying on orientation distributions and single-crystal elasticities of clay minerals could benefit from the direct mechanical assessments of stiffness and hardness offered by grid indentation experiments at micrometer and sub-micrometer length scales. In addition, the grid WDS technique implemented here for applications on shale rock proves to be a robust methodology for interpreting EPMA data. The combination of large datasets of WDS tests and the adequate design of the cluster analysis variables provides a means to investigate the chemical signature of the material of interest with heterogeneous microstructure. Such an approach, combined with indentation experiments, is well suited for the chemomechanical study of geomaterials such as oil shales and acidified carbonates.

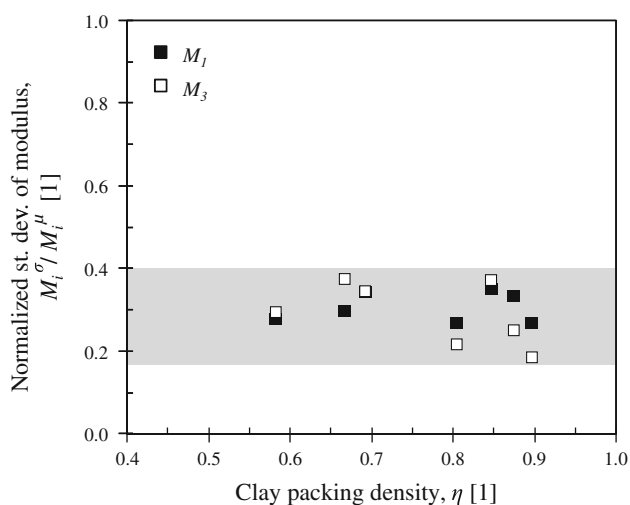


Fig. 16 Normalized standard deviation values M_i^σ/M_i^μ of the indentation moduli measured for the porous clay phase in shale materials introduced in Fig. 14. M_i^σ and M_i^μ values are detailed in Table 5

Acknowledgments We are grateful for the financial support of this study by the MIT-OU GeoGenome Industry Consortium (G2IC) directed by Prof. Younane Abohleiman of the integrated Poromechanics Institute (iPMI) of the University of Oklahoma at Norman. We thank Prof. Christopher Bobko (North Carolina State University) for providing the indentation data developed for G2IC shale materials and Dr. Nilanjan Chatterjee at the Electron Microprobe Facility, Department of Earth, Atmospheric, and Planetary Sciences, MIT for his guidance in the performing the WDS experiments. We also thank Prof. Manika Prasad (Colorado School of Mines) and an anonymous reviewer for their constructive comments which have enhanced the presentation of this manuscript.

References

1. Abohleiman Y, Tran M, Hoang S, Ortega JA, Ulm FJ (2009) Geomechanics field characterization of two prolific us mid-west gas plays with advanced wire-line logging tools. SPE annual technical conference 124428
2. Abuhaikal M, Ulm F-J (2011) Nanochemomechanical assessment of rice husk ash cement by WDS and nanoindentation. CEE research report R11-02, Massachusetts Institute of Technology
3. Ahmadov R, Vanorio T, Mavko G (2009) Confocal laser scanning and atomic-force microscopy in estimation of elastic properties of the organic-rich Bazhenov formation. *Lead Edge* 28(1):18–23
4. Bathija AP, Liang H, Lu N, Prasad M, Batzle ML (2009) Stressed swelling clay. *Geophysics* 74(4):A47–A52
5. Bennett RH, O'Brien NR, Hulbert MH (1991) Determinants of clay and shale microfabric signatures: processes and mechanisms. In: Bennett RH, O'Brien NR, Hulbert MH (eds) *Microstructure of fine grained sediments: from mud to shale*. Springer, New York, pp 5–32
6. Bobko C, Ulm F-J (2008) The nano-mechanical morphology of shale. *Mech Mater* 40(4–5):318–337
7. Bobko C, Ortega JA, Ulm F-J (2009) Comment on elastic modulus and hardness of muscovite and rectorite determined by nanoindentation. *Appl Clay Sci*
8. Bobko CP, Gathier B, Ortega JA, Ulm F-J, Borges L, Abohleiman YN (2010) The nanogranular origin of friction and cohesion in shale—a strength homogenization approach to interpretation of nanoindentation results. *Int J Numer Anal Methods Geomech*. doi:10.1002/nag.984
9. Broz ME, Cook RF, Whitney DL (2006) Microhardness, toughness, and modulus of Mohs scale minerals. *Am Miner* 91(1):135–142
10. Cariou S, Ulm F-J, Dormieux L (2008) Hardness-packing density scaling relations for cohesive-frictional porous materials. *J Mech Phys Solids* 56(3):924–952
11. Chen JJ, Sorelli L, Vandamme M, Ulm F-J, Chanvillard G (2010) A coupled nanoindentation/SEM-EDS study on low water/cement ratio portland cement paste: evidence for CSH/CA(OH)₂ nanocomposites. *J Am Ceram Soc* 93(5):1484–1493
12. Constantinides G, Ulm F-J (2007) The nanogranular nature of C–S–H. *J Mech Phys Solids* 55(1):64–90
13. Constantinides G, Ravi Chandran KS, Ulm FJ, Van Vliet KJ (2006) Grid indentation analysis of composite microstructure and mechanics: principles and validation. *Mater Sci Eng A* 430(1–2):189–202
14. Deer WA, Howie RA, Zussman J (1962) *Rock-forming minerals*, vol 3. Longmans, London
15. Deirieh A, Ortega JA, Ulm F-J (2011) Statistical nano-chemomechanical assessment of shale by wave dispersive spectroscopy and nanoindentation. CEE research report R11-03, Massachusetts Institute of Technology
16. Delafargue A, Ulm F-J (2004) Explicit approximations of the indentation modulus of elastically orthotropic solids for conical indenters. *Int J Solids Struct* 41(26):7351–7360
17. Dempster AP, Laird NM, Rubin DB (1977) Maximum likelihood from incomplete data via em algorithm. *J R Stat Soc Ser B Methodol* 39(1):1–38
18. Dilks A, Graham SC (1985) Quantitative mineralogical characterization of sandstones by back-scattered electron image analysis. *J Sediment Res* 55(3):347–355
19. Drouin D, Couture AR, Joly D, Tastet X, Aimez V, Gauvin R (2007) Casino v2.42—a fast and easy-to-use modeling tool for scanning electron microscopy and microanalysis users. *Scanning* 29(3):92–101
20. Fraley C, Raftery AE (1999) MCLUST: software for model-based cluster analysis. *J Classif* 16(2):297–306
21. Galin LA (1953) Contact problems in the theory of elasticity. Gostekhizdat, Moscow
22. Ganneau FP, Constantinides G, Ulm FJ (2006) Dual-indentation technique for the assessment of strength properties of cohesive-frictional materials. *Int J Solids Struct* 43(6):1727–1745
23. Goldstein J (2003) *Scanning electron microscopy and X-ray microanalysis*, 3rd edn. Kluwer, New York
24. Han D-H, Nur A, Morgan D (1986) Effects of porosity and clay content on wave velocities in sandstones. *Geophysics* 51(11):2093–2107
25. Heyliger P, Ledbetter H, Kim S (2003) Elastic constants of natural quartz. *J Acoust Soc Am* 114(2):644–650
26. Hornby BE, Schwartz LM, Hudson JA (1994) Anisotropic effective-medium modeling of the elastic properties of shales. *Geophysics* 59(10):1570–1583
27. Hughes JJ, Trtik P (2004) Micro-mechanical properties of cement paste measured by depth-sensing nanoindentation: a preliminary correlation of physical properties with phase type. *Mater Charact* 53(2–4):223–231
28. Jakobsen M, Hudson JA, Johansen TA (2003) *T* matrix approach to shale acoustics. *Geophys J Int* 154(2):533–558
29. Jin L, Rother G, Cole DR, Mildner DFR, Duffy CJ, Brantley SL (2011) Characterization of deep weathering and nanoporosity development in shale—a neutron study. *Am Miner* 96(4):498–512
30. Katti DR, Schmidt SR, Ghosh P, Katti KS (2005) Modeling the response of pyrophyllite interlayer to applied stress using steered molecular dynamics. *Clays Clay Miner* 53(2):171–178
31. Keller LM, Holzer L, Wepf R, Gasser P (2011) 3D geometry and topology of pore pathways in Opalinus clay: Implications for mass transport. *Appl Clay Sci* 52(1–2):85–95
32. Krinsley DH (1998) *Back-scattered scanning electron microscopy and image analysis of sediments and sedimentary rocks*. Cambridge University Press, Cambridge
33. Larsson PL, Giannakopoulos AE, Soderlund E, Rowcliffe DJ, Vestergaard R (1996) Analysis of berkovich indentation. *Int J Solids Struct* 33(2):221–248
34. Lee SY, Hyder LK, Alley PD (1991) Microstructural and mineralogical characterization of selected shales in support of nuclear waste repository studies. In: Bennett RH, Bryant WR, Hulbert MH (eds) *Microstructure of fine-grained sediments, from mud to shale*. Springer, New York, pp 545–560
35. Lonardelli I, Wenk H-R, Ren Y (2007) Preferred orientation and elastic anisotropy in shales. *Geophysics* 72(2):D33–D40
36. Loucks RG, Reed RM, Ruppel SC, Jarvie DM (2009) Morphology, genesis, and distribution of nanometer-scale pores in siliceous mudstones of the mississippian Barnett shale. *J Sediment Res* 79(12):848–861

37. Mba K, Prasad M, Batzle M (2010) The maturity of organic-rich shales using microimpedance analysis. SPE annual technical conference and exhibition, Florence, September 19–22, SPE 135569
38. McGee JJ, Keil K (2001) Application of electron probe microanalysis to the study of geological and planetary materials. *Microsc Microanal* 7(02):200–210
39. McLachlan GJ, Basford KE (1988) Mixture models: inference and applications to clustering. Marcel Dekker, New York
40. McLachlan GJ, Peel D (2001) Finite mixture models. Wiley, New York
41. Newman ACD (1987) Chemistry of clays and clay minerals. Longman Scientific and Technical, Harlow
42. Oliver W, Pharr G (1992) An improved technique for determining hardness and elastic modulus using load and displacement sensing indentation experiments. *J Mater Res* 7(6):1564–1583
43. Oliver WC, Pharr GM (2004) Measurement of hardness and elastic modulus by instrumented indentation: advances in understanding and refinements to methodology. *J Mater Res* 19(1):3–20
44. Ortega JA, Ulm F-J (2010) Microporomechanics modeling of shale. CEE research report R10-03, Massachusetts Institute of Technology
45. Ortega JA, Ulm F-J, Abousleiman Y (2007) The effect of the nanogranular nature of shale on their poroelastic behavior. *Acta Geotechnica* 2(3):155–182
46. Ortega JA, Ulm F-J, Abousleiman Y (2009) The nanogranular acoustic signature of shale. *Geophysics* 74(3):D65–D84
47. Ortega JA, Ulm FJ, Abousleiman Y (2010) The effect of particle shape and grain-scale properties of shale: a micromechanics approach. *Int J Numer Anal Methods Geomech* 34(11):1124–1156
48. Prasad M, Kopycinska M, Rabe U, Arnold W (2002) Measurement of Young's modulus of clay minerals using atomic force acoustic microscopy. *Geophys Res Lett* 29(8):13-1–13-4
49. Randall NX, Vandamme M, Ulm F-J (2009) Nanoindentation analysis as a two-dimensional tool for mapping the mechanical properties of complex surfaces. *J Mater Res* 24(3):679–690
50. Reed SJB (2006) Electron microprobe analysis and scanning electron microscopy in geology, 2nd edn. Cambridge University Press, Cambridge
51. Sarout J, Guéguen Y (2008) Anisotropy of elastic wave velocities in deformed shales: part 1—experimental results. *Geophysics* 73(5):D75–D89
52. Sneddon IN (1965) The relation between load and penetration in the axisymmetric boussinesq problem for a punch of arbitrary profile. *Int J Eng Sci* 3(1):47–57
53. Tai K, Ulm F-J, Ortiz C (2006) Nanogranular origins of the strength of bone. *Nano Lett* 6(11):2520–2525
54. Tovey NK, Krinsley DH (1991) Mineralogical mapping of scanning electron micrographs. *Sediment Geol* 75(1–2):109–123
55. Tovey NK, Krinsley DH, Dent DL, Corbett WM (1992) Techniques to quantitatively study the microfabric of soils. *Geoderma* 53(3–4):217–235
56. Ulm F-J, Abousleiman Y (2006) The nanogranular nature of shale. *Acta Geotechnica* 1(2):77–88
57. Ulm F-J, Delafargue A, Constantinides G (2005) Experimental microporomechanics. In: Dormieux L, Ulm F-J (eds) Applied micromechanics of porous materials. Springer, Wien, pp 207–288
58. Ulm FJ, Vandamme M, Bobko C, Ortega JA, Tai K, Ortiz C (2007) Statistical indentation techniques for hydrated nanocomposites: concrete, bone, and shale. *J Am Ceram Soc* 90(9):2677–2692
59. Vandamme M, Ulm F-J (2009) Nanogranular origin of concrete creep. *Proc Natl Acad Sci* 106(26):10552–10557
60. Vanzo J, Ulm F-J (2009) A nanochemomechanical investigation of carbonated cement paste. CEE research report R09-01, Massachusetts Institute of Technology
61. Voltolini M, Wenk H-R, Mondol NH, Bjorlykke K, Jahren J (2009) Anisotropy of experimentally compressed kaolinite–illite–quartz mixtures. *Geophysics* 74(1):D13–D23
62. Weaver CE, Pollard LD (1973) The chemistry of clay minerals. Elsevier, Amsterdam
63. Wenk H-R, Voltolini M, Mazurek M, Van Loon LR, Vinsot A (2008) Preferred orientations and anisotropy in shales: Callovo–Oxfordian shale (France) and Opalinus clay (Switzerland). *Clays Clay Miner* 56(3):285–306
64. Whitney DL, Broz M, Cook RF (2007) Hardness, toughness, and modulus of some common metamorphic minerals. *Am Miner* 92(2–3):281–288
65. World Energy Council (2007) Survey of energy resources. Technical report. World Energy Council
66. Zargari S, Prasad M, Mba K, Mattson E (2011) Organic maturity, hydrous pyrolysis, and elastic property in shales. Canadian unconventional resources conference, Calgary, November 15–17, SPE 149403
67. Zhang G, Wei Z, Ferrell RE (2009) Elastic modulus and hardness of muscovite and rectorite determined by nanoindentation. *Appl Clay Sci* 43(2):271–281
68. Zhang G, Wei Z, Ferrell RE, Guggenheim S, Cygan RT, Luo J (2010) Evaluation of the elasticity normal to the basal plane of non-expandable 2:1 phyllosilicate minerals by nanoindentation. *Am Miner* 95(5–6):863–869